Jagiellonian University
Faculty of Physics, Astronomy and Applied Computer Science

STUDIES OF QUANTUM ENTANGLEMENT IN PAIR OF HIGH ENERGETIC PHOTONS FROM e^+e^- ANNIHILATION

Ph.D. thesis

Author:
Nikodem Krawczyk

Thesis supervisor:
prof. dr hab. Paweł Moskal

Cracow, 2023

Wydział Fizyki, Astronomii i Informatyki Stosowanej
Uniwersytet Jagielloński

Oświadczenie

Ja niżej podpisany Nikodem Krawczyk (nr indeksu: 1051962) doktorant Wydziału Fizyki, Astronomii i Informatyki Stosowanej Uniwersytetu Jagiellońskiego oświadczam, że przedłożona przeze mnie rozprawa doktorska pt. „Studies of quantum entanglement in pair of high energetic photons from e^+e^- annihilation" jest oryginalna i przedstawia wyniki badań wykonanych przeze mnie osobiście, pod kierunkiem prof. dr hab. Pawła Moskala. Pracę napisałam/napisałem samodzielnie.

Oświadczam, że moja rozprawa doktorska została opracowana zgodnie z Ustawą o prawie autorskim i prawach pokrewnych z dnia 4 lutego 1994 r. (Dziennik Ustaw 1994 nr 24 poz. 83 wraz z późniejszymi zmianami).

Jestem świadoma/świadom, że niezgodność niniejszego oświadczenia z prawdą ujawniona w dowolnym czasie, niezależnie od skutków prawnych wynikających z ww. ustawy, może spowodować unieważnienie stopnia nabytego na podstawie tej rozprawy.

Kraków, dnia .....

podpis doktoranta

Abstract

In this thesis we have discussed the measurement of the distribution of the angle between scattering planes of photons originating from para-positronium decays using J-PET detector. We have compared the results of the measurements against two hypotheses - that the decaying state is entangled and that is separable.

In the performed experiment photons from para-positronium decay undergo Compton scatterings inside the plastic scintillator and the scattering direction depends on the photon's polarization. An access to the polarization degree of freedom in the case of measurements of photons from the decays of positronium opens new perspectives for studies of the discrete symmetries and quantum entanglement of high energy photons. Studies of the relative angle between two photons polarizations can also be used in the background suppression in Positron Emmision Tomography imaging.

In order to estimate detector efficiency for the detection of the angle between scattering planes we have performed Monte Carlo simulations of polarized photons inside the J-PET detector for two assumptions - that the photons are entangled and that they are separable.

We have also performed a measurement using J-PET detector where sodium source sandwiched between porous material was placed in the center of the detector. The decays of the resulting para-positronia in porous polymer were measured and the results of this measurement were then corrected by the simulated efficiency of the detector.

Finally we have compared experimentally determined distributions of the relative angle between scattering planes of annihilation photons with the theoretical distributions for two assumptions - that the decaying state is entangled and that it is separable. We have shown that the experimental results are in better agreement with the prediction obtained under assumption of the entangled states than with the prediction obtained under the assumption of separable state.

Abstrakt

W tej pracy omówiliśmy pomiar rozkładu kąta pomiędzy płaszczyznami rozpraszania fotonów pochodzących z rozpadów para-pozytonium przy użyciu detektora J-PET. Wyniki pomiarów porównaliśmy z dwiema hipotezami – że stan ulegający rozpadowi jest splątany, oraz że jest separowalny.

W wykonanym eksperymencie fotony pochodzące z rozpadu para-pozytonium ulegają rozproszeniom Comptona wewnątrz plastikowego scyntylatora, a kierunek rozpraszania zależy od polaryzacji fotonu. Dostęp do polaryzacyjnego stopnia swobody w przypadku pomiarów fotonów z rozpadów pozytonu otwiera nowe perspektywy badań takich jak symetrie dyskretne i splątanie kwantowe wielu wysoko energetycznych fotonów. Badania względnego kąta między polaryzacją dwóch fotonów można również wykorzystać do tłumienia tła w obrazowaniu Pozytonowej Tomografii Emisyjnej .

Aby oszacować wydajność detektora w detekcji kąta pomiędzy płaszczyznami rozpraszania, przeprowadziliśmy symulacje Monte Carlo spolaryzowanych fotonów wewnątrz detektora J-PET przy dwóch założeniach - że fotony są splątane i że są separowalne.

Przeprowadziliśmy również pomiar za pomocą detektora J-PET, w którym źródło sodu otoczone porowatym materiałem umieszczono w środku detektora, następnie zmierzono rozpady powstałego para-pozytonium w porowatym materiale, a wyniki tego pomiaru skorygowano za pomocą wysymulowanej wydajności detektora.

Na koniec porównaliśmy wyniki zmierzonego rozkładu kąta między płaszczyznami polaryzacji anihilacyjnych fotonów z rozkładami teoretycznymi dla dwóch założeń – że stan rozpadu jest splątany i że jest separowalny. Pokazaliśmy, że wyniki eksperymantalne są w lepszej zgodności z wynikami teoretycznymi z założeniami dla stanów splątanych niż z wynikami otrzymanymi przy założeniu stanu separowalnego.

Contents

1 Introduction

Aim of this thesis was to study decays of positronia into photons. Specifically distribution between photon's scattering planes in back-to-back decays from para-positronium in J-PET detector was investigated by comparing measured distributions of the angle between scattering planes with simulated distributions of the same angle for two different hypotheses - that the decaying state is: a) separable, b) entangled.

Positronium is a unique, purely leptonic system that decays into multiple photons. Studies of those photons polarizations allows investigations of discreete symmetries breaking [1, 2], multipartite quantum entanglement [3, 4, 5, 6] and background suppression in PET imaging [7, 8, 9, 10, 11].

Photons from the e^+e^- annihilation interact in plastic scintillators predominantly via the Compton effect and in the J-PET detector a few percent of them undergo secondary scatterings. Events with multiple scatterings may be used to estimate the linear polarization of the initial photon at the moment of its interaction. Taking into account that the scattering is most likely at an angle orthogonal to the polarization we may estimate polarization direction [1]: $\hat{\epsilon} = \hat{k} \times \hat{k}'$ where $\hat{k}$ and $\hat{k}'$ denotes the momentum unit vectors of the photon before and after the Compton scattering, respectively. Access to the polarization degree of freedom in the case of measurements of photons from the decays of positronium opens new perspectives for studies of the discrete symmetries [1, 2] and multipartite quantum entanglement [3, 6].

J-PET is a multipurpose detector designed for the development of medical imaging [12, 13, 14, 15, 16, 17], for studies of discrete symmetries in decays of positronium atoms [1, 18], as well as for investigations of multipartite quantum entanglement of photons originating from positronium annihilation [3, 4, 5]. J-PET is built from 192 plastic scintillator strips arranged axially in three cylindrical layers [19], here we only briefly outline it's main features. Photons interacting in a scintilators create light signals which are converted to electrical signals by photomultipliers placed at opposite ends of each strip [12]. Position and time of the interaction in the detector material are determined based on the arrival time of light signals at both ends of the scintillator strips. The signals are probed in the voltage domain with the accuracy of about 30 ps by a newly developed type of front-end electronics [20]. The data are collected by the novel trigger-less and reconfigurable data acquisition system [21] and analyzed by using dedicated analysis framweork [22, 23].

In this thesis we have investigated the distribution of the angle between scattering planes in the double Compton scattering of a pair of photons from para-positronium (see fig. 1.1 and fig. 1.2).

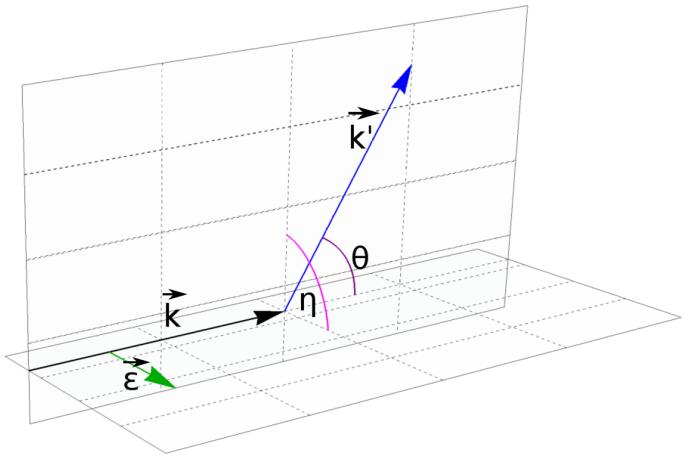

Figure 1.1: Compton scattering scheme. Photon with initial momentum $\vec{k}$ is scattered at Compton scattering angle θ. Scattered momentum $\vec{k'}$ and initial momentum span plane called scattering plane. Initial photon's polarization $\vec{\varepsilon}$ and initial momentum span polarization plane. Azimuthal scattering angle η is the angle between scattering and polarization planes (image previously used by author in [24].)

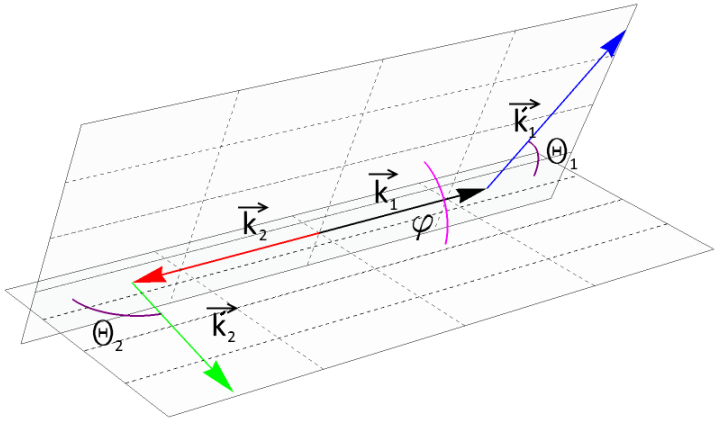

Figure 1.2: Compton scattering of two photons from back-to-back decay. In the experiment we can measure initial photon momenta directions ($\vec{k_1}$ and $\vec{k_2}$) and scattered ($\vec{k_1'}$ and $\vec{k_2'}$) momenta. Scattering direction depends on photon's polarization (eq. 3.14) and since photons polarizatons are correlated (eq. 3.13) angle between scattering planes φ is an estimate of relative angle between initial photons polarizations (image previously used by author in [24]).

We have prepared Monte Carlo simulation of the J-PET detector and simulated propagation and scattering of photons originating from para-positronium decay with two assumptions - that photons are entangled and that photons are separable but correlated. We have used those simulations to adjust selection criteria for measured data as well as determine detector response and it's efficiency. We have performed a measurement of the angle between scattering planes of two photons by

placing sodium ^{22}Na positron emitter in the center of the detector. Finally we have compared measured distribution with theoretical distributions for two hypotheses - that photons after para-positronium decay are entangled and that they are separable.

The structure of this thesis goes as follows: in chapter 2 we will discuss previous experiments measuring correlations between polarizations of photons from positronium decay, in chapter 3 we will lay down theoretical foundations regarding photons originating from positronium decay and their scatterings, in chapter 4 we will describe in details detector setup and performed measurement, in chapter 5 we will discuss performed Monte Carlo simulations of the J-PET detector response, and will use it to calculate detection corrections, in chapter 6 we will perform analysis of the measured data and finally in chapter 7 we will show obtained results.

Author contribution

Author of this thesis was a part of both teams responsible for the development of the software used in this thesis, that is J-PET Framework as well as Monte Carlo simulation package based on Geant4. Author also took part in the setup of the measurement and collection of raw data used in this thesis. Monte Carlo simulations used in this thesis, data selection and data analysis were performed solely by author oh this thesis. In summary, the author was deeply involved in all stages of the research process — from software development to experimental setup, data collection, Monte Carlo simulations, data selection, and analysis.

This work was supported by Foundation for Polish Science through grant
TEAM POIR.04.04.00-00 - 420417, the National Science Centre, Poland (NCN) through grant No. 2021/42/A/ST2/00423. The work also has been supported by a grant from the SciMat and qLife Priority Research Areas under the Strategic Programme Excellence Initiative at the Jagiellonian University.

Previous experiments

2

2.1 Earliest experiments

In year 1946 J.A. Wheeler published an article in which he discussed polarizations of photons originating from e^+e^- decays [25]. He stated that if one of the photons is linearly polarized in one plane then the second photon with the same momentum in the opposite direction will be linearly polarized in the perpendicular plane. In order to confirm his hypothesis Wheeler proposed an experiment in which a slow positron interacts with an electron at rest to produce two photons. In this experiment azimuthal correlation between the polarization of two photons undergoing Compton scattering was measured. Compton scattering was chosen as a polarization analyzer for high-energy $511keV$ photons. According to Klein-Nishina formula [26], photon will most likely scatter perpendicular to the direction of its linear polarization (which equals to $\eta = 90°$ in fig. 1.1), similarly other photon will scatter at it's preferred azimuthal angle. Therefore, Compton scattering of both photons will result in preferential registration of the photons with a chosen polarization. The correlation of polarizations can be measured by calculating the ratio when the relative azimuthal angles of scattered photons is perpendicular to each other (labeled as $N_\perp$; $\varphi = 90°$ in fig. 1.2) to those scattered parallel (labeled $N_\parallel$). Wheeler also made prediction that maximum value of this ratio should be expected at Compton scattering angles of $\theta = 74.3°$, however year later M. Pryce and J. Ward noticed [27] an error in Wheeler's prediction of the two-photon wave function of entangled photons — the interference term was neglected. They made a correction to this and claimed that the maximum ratio $\frac{N_\perp}{N_\parallel}$ would be expected at Compton scattering angles of $\theta = 82°$. They have also described an experimental setup to perform measurement proposed by Wheeler and derived the double differential cross-section for the scattering of two linearly polarized photons by θ_1 and θ_2 at the corresponding azimuthal angles ϕ_1 and ϕ_2 [27]. This cross section is given as:

$$\frac{d^2\sigma(\theta_1,\phi_1,\theta_2,\phi_2)}{d\Omega_1 d\Omega_2} = \frac{r_e^4}{14}\left[A(\theta_1,\theta_2) - B(\theta_1,\theta_2)\cos(2\Delta\phi)\right] \tag{2.1}$$

where:

$$\begin{aligned} A(\theta_1,\theta_2) &= \frac{[(1-\cos\theta_1)^3+2][(1-\cos\theta_2)^3+2]}{(2-\cos\theta_1)^3(2-\cos\theta_2)^3}, \\ B(\theta_1,\theta_2) &= \frac{\sin^2\theta_1\sin^2\theta_2}{(2-\cos\theta_1)^2(2-\cos\theta_2)^2}, \end{aligned} \tag{2.2}$$

where θ_1 and θ_2 are Compton scattering angles for first and second photon respectively, $\Delta\phi$ is a relative azimuthal angle between two scattering photons ($\phi_1 - \phi_2$)

and r_e is classical electron radius. Similar equation was also independently derived by Snyder et al. [28].

Next year, based on proposed experimental setup, two experiments were performed by Bleuler et al. [29] and Hanna [30]. Both experiments observed a correlation between linear polarizations of two photons undergoing Compton scatterings. Experimentally obtained ratio of the correlation was however in both experiments consistently lower than theoretically predicted value using equation (2.1). Hannah made few observations that could account for the discrepancies between theoretically predicted and experimentally measured values, that is: (i) absence of low density scatters, (ii) lack of an efficient gamma ray counter, (iii) limited geometric acceptance for studying events of interest. This experiment was then repeated in 1950 by Wu and Shakanov [31] with an improved aluminium scatter and newly developed gamma ray detectors based on anthracene crystals coupled to RCA 5819 photo-multiplier tubes. Anthracene based scintillator counters had ten times better efficiency that Geiger counters used in previous experiments [29, 30]. Wu and Shakanov obtained an experimental result of correlation ratio of 2.04 ± 0.08 which was consistent with theoretically predicted value of 2.0. It needs to be emphasized that all those experiments had different experimental configuration therefore required a modification to the Pyrc-Ward formula (2.1) to account for the corrections for geometric effects before comparing them to the theoretical results.

Two more experiments were performed later, first one conducted in 1960 by Langhoff [32], who reported the results of thorough measurements with improved geometry by measuring the correlation ratio at various azimuthal angles and a good agreement was obtained between estimated theoretical prediction (2.48 ± 0.02) and the experimentally measured value (2.47 ± 0.07) for the polar scattering angle $\theta = 82°$. Second study was performed by Kasday et al. [33] in 1975 where they explicitly applied several sources of corrections that could be necessary for the correct estimation of such correlations. They proposed to rewrite equation (2.1) as:

$$P(\Delta\phi) = k(1 - \nu(\theta_1, \theta_2)\cos(2\Delta\phi)), \tag{2.3}$$

where

$$\begin{aligned} k &= \frac{r_e^4 A(\theta_1, \theta_2)}{16}, \\ \nu &= \frac{B(\theta_1, \theta_2)}{A(\theta_1, \theta_2)}. \end{aligned} \tag{2.4}$$

Functions k and ν are sensitive to Compton scattering angles and the correlation ratio (R) of the linear polarization of annihilation photons can be measured by calculating it when $\Delta\phi = \pm 90°$ and $\Delta\phi = 0°$. Expression for R is then defined as:

$$R(\Delta\phi) = \frac{P(\Delta\phi = \pm 90°)}{P(\Delta\phi = 0°)} = \frac{1 + \nu}{1 - \nu} \tag{2.5}$$

for which the maximum value is 2.85 at Compton scattering angles $\theta_1 = \theta_2 = 82°$.

In 1957 Bohm and Aharnov argued [34] that the possibility of experimentaly observing correlations between the linear polarizations of annihilation photons could be considered as a similar case of quantum entanglement as discussed by Einstein, Podolsky and Rosen [35]. Following the experimental setup of Wu et al. [31] Bohm and Aharnov derived result that allowed the use of the values of R to establish upper limits for two hypotheses: (i) entangled state of 2 linearly polarized photons, with spins ± 1 for which wave function can be expressed as $|\psi\rangle = \frac{1}{\sqrt{2}}(|+\rangle_1 |-\rangle_2 - |-\rangle_1 |+\rangle_2)$ and (ii) separable state for which wave function does not overlap but polarizations are orthogonally correlated. Upper limit for the entangled state was calculated with value of 2.85 while value for separable state was calculated to be less than 2. In 1976 Wilson et al. [36] measured the influence of the distance between Compton polarimeters and annihilation point on the correlation ratio R and reported no significant change of this value even at the distance of $2.5m$ therefore such measured correlation between photons emitted from e^+e^- annihilations in the back-to-back direction and forming a line-of-response (LOR) could be used to remove unwanted coincidences accepted during imaging of the source of annihilation [37, 38].

2.2 Recent experiments

In recent years three experiments were performed, by Watts et al. [8], Abdurshitov et al. [9] and Parashari et al. [11]. Watts et al. demonstrated use of entangled polarization correlations to distinguish true events (in which no photon scattered before it was detected) and scattered events (in which at least one photon was scattered before detection therefore causing a decoherence). It was shown that in the case of the decoherence correlation between the relative polarization amplitudes was much lower than in the case of entangled photons, as a consequence, by selecting only those events in which the relative polarization is entangled the image quality can be significantly improved by suppressing the background. They have also determined the exact value of the upper limit for the separable state of 1.63 by introducing the correction to the formula derived in Bohm's paper [34] (details of which can be found in supplementary note in Watts et al. [8]). Abdurshitov et al. reported that regardless of the initial state (entangled or decoherence) same distribution of polarizations correlations were measured. This has raised a question as to whether the measured correlation between the polarization of annihilation photons can be considered a unique signature for distinguishing the origin of the annihilation photons from entangled or separable states. In all three studies different detector setus were used to measure the correlations ratio based on Compton scatterings, however, the methodologies used to define entangled and decoherent states were nearly identical. Below we will discuss those experiments in more details.

2.2.1 York experiment

In their experiment Watts et al. [8] tested the hypothesis proposed by Bohm and Aharonov [34]. In the experiment two cadmium-zinc-telluride (CZT) detectors were placed 8.7 cm apart, each detector was a 1cm cube divided into 121 pixels of a size $0.8 \times 0.8\text{mm}^2$. In the middle of the two detection modules sodium ^{22}Na with the activity of 170 kBq was placed. Source was placed in a plastic housing and emitted photons with energy of 511 keV in the opposite direction. Measurement was performed with two different experimental setups: first when the detectors were placed along the axial alignment of the source to register annihilation photons and the corresponding scattered photons and second, when one of the detectors was rotated off source alignment axis by 33° (see 2.1) and scattering medium was placed along the path of the annihilation photon. Second detection setup was measuring the influence of the prior scattering of photon (therefore loss of entanglement) on the correlation ratio (R).

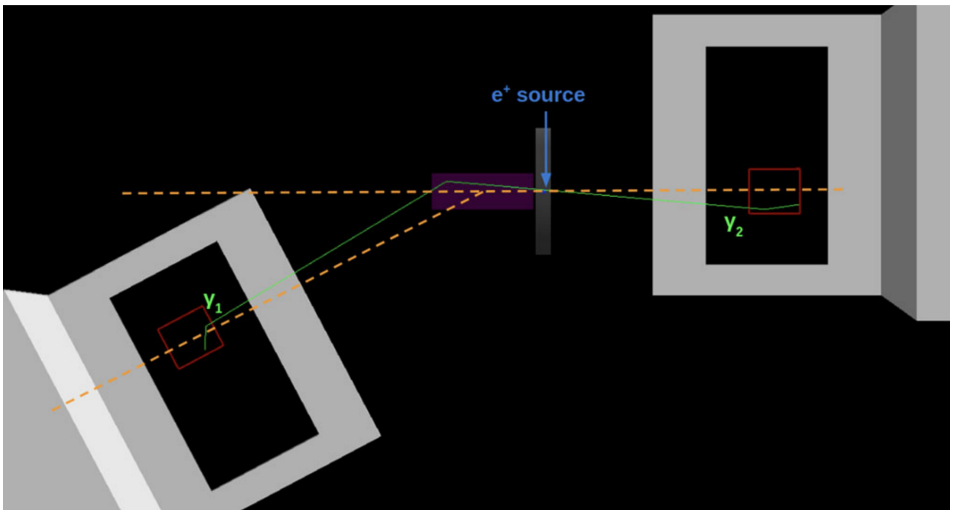

Figure 2.1: Setup of the experiment performed by Watts et al. (graphic taken from [8]). Cadmium-zinc-telluride (CZT) crystals (red) are shown along with their support structures (grey) and the nylon scattering medium (purple). Solid green lines represent annihilation photons in a typical scattering event. One of the photons Compton scatters in the nylon scattering medium (purple) and the subsequent photons both scatter within the CZT crystals.

In the first experimental setup Watts et al. obtained a result of $R = 1.85 \pm 0.04$ for a selected scattering range of $70^\circ - 110^\circ$ which is less then theoretically predicted value for entanglement (2.85) [33], but more that theoretically predicted upper limit for separable states [34, 8]. Measured distribution of $\Delta\phi$ was well described by quantum entangled PET (QE-PET) simulation results. QE-PET was developed based on Geant4 toolkit which incorporates the entanglement formalism for the primary interaction of the annihilation photons with the detector instead of standard Klein-Nishina formalism for polarised photons (see methods in [8] for details). With a more narrow range of $93^\circ - 103^\circ$ value of R reached 1.95 ± 0.07.

In the second detection setup significant suppression was observed for the decoherent state in both measured and simulated data. Due to a large statistical uncertainty which could come from small aperture for the detecting scattered photons it is difficult to draw any strong conclusions to whether the measured relative correlations have been suppressed by a hypothesis-based formalism [34] or whether more advanced measurements with broader geometric acceptance are required. In summary it was reported that kinematics of Compton scattering in orthogonally entangled annihilation photons is different from the kinematics in which entanglement is considered lost due to the prior scattering of one of the photons.

2.2.2 Moscow experiment

Abdurashitov et al. reported experimental results [9] that contradicted results presented by Watts et al. [8]. Both experiments were performed using the same methodology: when the photons were considered entangled in their relative linear polarizations and when introducing decoherence by forcing one of the photons from back-to-back pair to be scattered before it was registered in the detector. In the experiment Abdurashitov et al. used two Compton polarimeters, each consisting of 16 NaI(Tl) of a size $5 \times 5cm^2$ spaced $70cm$ apart and a plastic scatterer (transparent cylinder) in the center, with equal distance from all NaI crystals. Annihilation photons were produced by β^+ emitter, ^{22}Na with an activity of 50MBq which was placed in a lead shield with a perforated cylindrical colimator. Decoherence was introduced by placing gadolinium–aluminum–gallium–garnet (GAGG) along the path of one of the annihilation photons. Events with and without interaction in GAGG were labeled as decoherent and entangled respectively. In the experimental setup photons interacted in the scatterers and the scattered photons were registered in the NaI(Tl) counters of the polarimeters (Fig. 2.2).

The differential cross section for Compton scattering of a linearly polarized photon can be calculated using Klein-Nishina formula [26]:

$$\begin{aligned}\frac{d\sigma}{d\Omega}(\theta,\eta) &= r_e^2\epsilon^2\left(\epsilon+\frac{1}{\epsilon}-2\sin^2\theta\cos^2\eta\right)\\ &= r_e^2\epsilon^2\left(\epsilon+\frac{1}{\epsilon}-\sin^2\theta\right)\left[1-\frac{\sin^2\theta\cos\left(2\eta\right)}{\epsilon+\frac{1}{\epsilon}-\sin^2\theta}\right]\\ &= r_e^2\left(1-\alpha(\theta)\cos\left(2\eta\right)\right),\end{aligned} \tag{2.6}$$

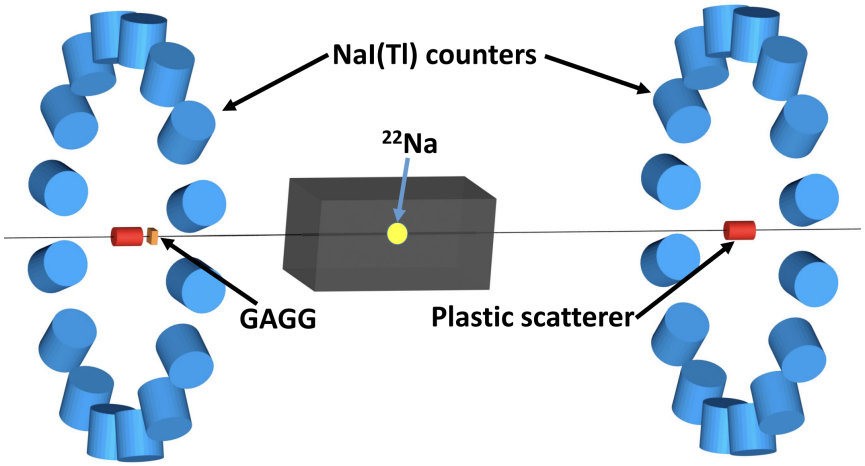

Figure 2.2: Setup of the experiment performed by Abdurashitov et al. (graphic taken from [9]). Two Compton polarimeters made of 16 NaI(Tl) counters and a plastic scatterer are placed on both sides of sodium ^{22}Na source. An scatterer of GAGG scintillator is placed in one arm to produce the decoherent photons.

where ϵ is the ratio of scattered to incident photon energy $\left(\frac{E'}{E}\right)$, θ is the Compton scattering angle, η is the azimuthal angle (angle between scattering plane and the direction of linear polarization of the incident photon) and:

$$k = \epsilon^2 \left(\epsilon + \frac{1}{\epsilon} - \sin^2\theta\right), \tag{2.7}$$

$$\alpha(\theta) = \frac{\sin^2\theta}{\epsilon + \frac{1}{\epsilon} - \sin^2\theta}. \tag{2.8}$$

Analyzing power of Compton polarimeter can be described as [39]:

$$\begin{aligned} A(E,\theta) &= \frac{\frac{d\sigma}{d\Omega}(\theta, \phi = 90^\circ) - \frac{d\sigma}{d\Omega}(\theta, \phi = 0^\circ)}{\frac{d\sigma}{d\Omega}(\theta, \phi = 90^\circ) + \frac{d\sigma}{d\Omega}(\theta, \phi = 0^\circ)} \\ &= \frac{sin^2\theta}{\frac{E'}{E} + \frac{E}{E'} - \sin^2\theta} = \alpha(\theta). \end{aligned} \tag{2.9}$$

For the photon of energy 511keV parameter A reaches a maximal value of $A = 0.69$ for Compton scattering angle of $\theta = 82^\circ$ (see Fig. 2.3). Probability of Compton scattering of two orthogonally polarized photons scattering at the angles θ_1 and θ_2 can be written in terms of analyzing power of Compton polarimeters [9]:

$$P(E_1, E_2, \Delta\phi) = r_e^2 k_1 k_2 \left[1 - \alpha(\theta_1)\alpha(\theta_2)\cos(2\Delta\phi))\right], \tag{2.10}$$

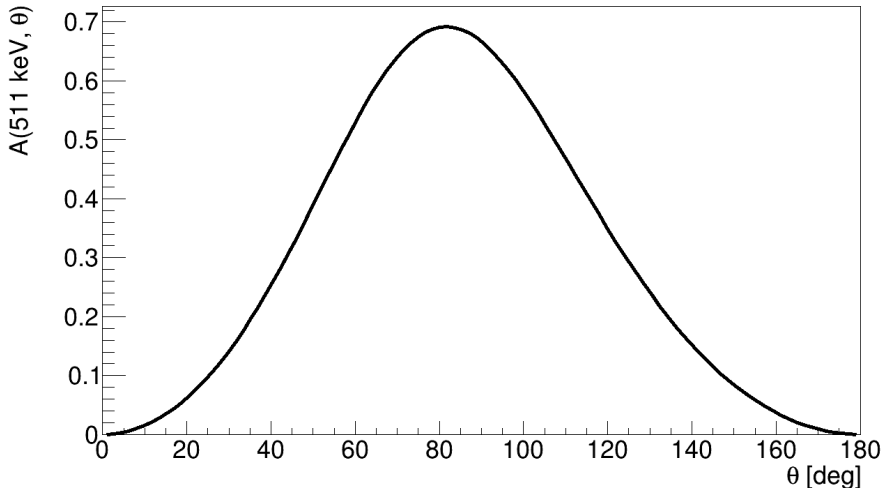

Figure 2.3: Distribution of analysing power of Compton polarimeter for photons with initial energy of 511 keV.

and the polarization modulation factor (μ) estimating the relative polarization of annihilation photons can be calculated as [4, 40]:

$$\mu = \frac{P(\Delta\phi = 90^{\circ}) - P(\Delta\phi = 0^{\circ})}{P(\Delta\phi = 90^{\circ}) + P(\Delta\phi = 0^{\circ})} = \alpha(\theta_1)\alpha(\theta_2). \tag{2.11}$$

Modulation factor is equal to the product of the analyzing powers of the individual polarimeters. Maximal modulation is equal to $\mu = 0.49$ for Compton scattering angles $\theta_1 = \theta_2 = 82^{\circ}$. Correlation ratio R can be expressed using modulation factor as $R = \frac{1+\mu}{1-\mu}$. Modulation factor μ obtained by Abdurashitov et al. is equivalent to correlation ratio 2.5 obtained by Kasday et al. [33]. Experimentally obtained value of μ was 0.41 which corresponds to $R \approx 2.39$ and proved to be better approximation to the theoretically predicted value of $R = 2.85$. It should be noted that in the paper of Abdurashitov et al.[9] observed no difference for the μ distribution for entangled and decoherent states which indicates that Compton kinematics remainded identical in both cases as was predicted in [4].

2.2.3 Zagreb experiment

Due to different conclusions arising from work of Watts et al. [8]. and Abdurashitov et al. [9] regarding the strength of the correlation after the scattering S. Parashari et al. [11] performed an experiment trying to resolve this discrepentancy called "decoherence puzzle" [7]. Their detection setup is based on the single-layer gamma-ray polarimeter concept [10], that consists of two single-layer gamma polarimeters and a scatterer scintillator (see Fig. 2.4). Each polarimeter encompasses 8 × 8 gadolinium–aluminum–gallium–garnet doped with cerium (GAGG:Ce) scintillator matrix with crystal dimensions $1.9 \times 1.9 \times 20\text{mm}^3$ and 2.2 mm pitch. The matrix is read out on one end by a silicon-photomultiplier (SiPM) array, with one-to-one

match of crystals and SiPMs. The mean energy resolution (FWHM) of the GAGG:Ce detectors was $8.1 \pm 0.5\%$ at 511 keV. The scatterer was a single scintillating crystal of GAGG:Ce with the dimensions of $3.0 \times 3.0 \times 20$ mm^3 wrapped with teflon which was read out by one SiPM of a 8x8 SiPM array (KETEK PA3325) and its energy resolution was $12.1 \pm 0.3\%$ at 511 keV. Sodium ^{22}Na source with 1 mm diameter and activity of $\approx$ 370 kBq was placed 1 cm from the scatterer between the scatterer and the detector that was fixed in place. Other detector was free to move along the arc allowing for selection of different Compton scattering angles.

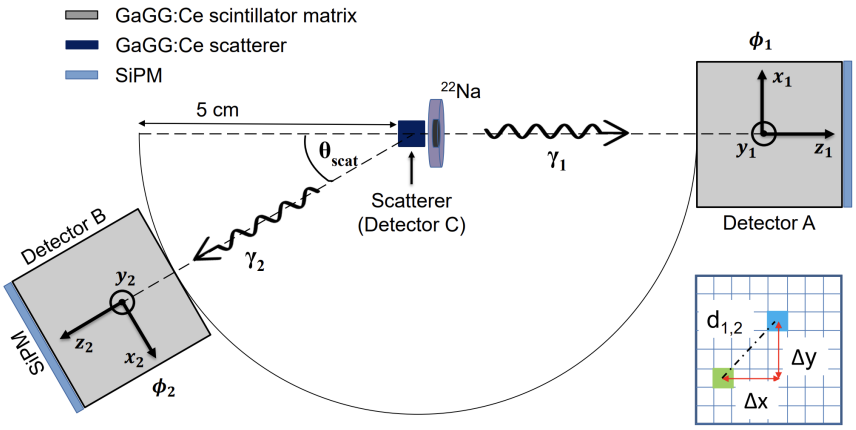

Figure 2.4: Setup of the experiment performed by Parashari et al. (graphics taken from [11]). Two polarimeters (called Detector A and B) made of 8x8 GAGG:Ce scintillator matrix with SiPM array readout were placed at a fixed distance 5cm away from the scatterer (detector C) that was meant to introduce decoherence into a system. Detector B was free to move along the arc allowing for the selection of different Compton scattering angles (θ_{scat}). Scatterer was made out of single scintillating crystal of GAGG:Ce wrapped with teflon and read out by one SiPM array. Sodium ^{22}Na was placed 1cm from the scatterer between the scatterer and Detector A. The azimuthal angles $\phi_{1,2}$ and the inter-pixel distances $d_{1,2}$ are deduced from the relative positions of the fired pixels in the respective module.

In the experiment one of the detectors was detecting the photons coming directly from the annihilation event, while second one was detecting the photon after scattering in the scatterer detector which was introduced to induce decoherence by Compton scattering and to tag such events. Compton scattering angle and azimuthal scattering angle were calculated as follows:

$$\begin{aligned} \theta &= \operatorname{acos}\left(\frac{m_e c^2}{E_{px_1} + E_{px_2}} - \frac{m_e c^2}{E_{px_2}} + 1\right) \\ \phi &= \operatorname{atan}\left(\frac{\Delta y}{\Delta x}\right), \end{aligned} \tag{2.12}$$

where $E_{px_{1,2}}$ stands for energy deposited in pixel 1 and 2, Δx and Δy are the distances of the fired pixel centers in the plane perpendicular to the longer crystal axis (see Fig. 2.4). For the events that satisfy the Compton selection criteria and for a given range of the reconstructed angles $\theta_{1,2}$, distribution of the azimuthal angle differences $N(\phi_1 - \phi_2)$ was obtained, where $\phi_{1,2}$ are the azimuthal angles of the Compton events in Detector A and B, respectively. The $N(\phi_1 - \phi_2)$ distributions were then corrected for detector acceptance as:

$$N_{corr}(\phi_1 - \phi_2) = \frac{N(\phi_1 - \phi_2)}{N_{mix}(\phi_1 - \phi_2)} \tag{2.13}$$

The N_{mix} is the acceptance determined by event-mixing technique [10, 41] where $\phi_1 - \phi_2$ is obtained by taking ϕ_1 and ϕ_2 from different randomly chosen events. The modulation factor, μ, is determined by fitting the acceptance-corrected distribution, $N_{corr}(\phi_1 - \phi_2)$, with $N_{corr}(\phi_1 - \phi_2) = M[1 - \mu\cos(2(\phi_1 - \phi_2))]$ where M corresponds to the average amplitude of the distribution. Polarization modulation factor was measured to be $\mu = 0.31 \pm 0.01$ for the case with no interactions in the scatterer and did not significantly differ when one of the photons scattered in a scatterer at Compton angle θ_{scat} in range between $(0°, 30°)$ which is in line with a result of Abdurashitov et al. [9] and differs from result of Watts et al. [8]. It is worth noting that even though the conclusion of the experiment seems to be in line with the experiment of Abdurashitov et al. the measured value of modulation factor is different from $\mu = 0.41$ obtained by Abdurashitov et al. [9].

Theoretical description

3

3.1 Positronium

Electron and positron can form unstable bound state called positronium, first experimentally confrmed by Martin Deutsch in 1951 [42]. Positronium as a two-body system has similar energy level structure to hydrogen with the Bohr radius, twice as large as hydrogen, $r_b = 0.106$ nm. The combination of positron and electron spins allows for the formation of positronium in one of two states differing in the total spin (S). Spin of positronium is a linear combination of electron and positron spins:

$$\begin{aligned} |S=1, S_z=-1\rangle &= |\uparrow\rangle\,|\uparrow\rangle \\ |S=1, S_z=0\rangle &= \frac{1}{\sqrt{2}}\left(|\uparrow\rangle\,|\downarrow\rangle + |\downarrow\rangle\,|\uparrow\rangle\right) \\ |S=1, S_z=1\rangle &= |\downarrow\rangle\,|\downarrow\rangle \\ |S=0, S_z=0\rangle &= \frac{1}{\sqrt{2}}\left(|\uparrow\rangle\,|\downarrow\rangle - |\downarrow\rangle\,|\uparrow\rangle\right) \end{aligned} \tag{3.1}$$

where $|\uparrow\rangle$ and $|\downarrow\rangle$ denote $S_z = +\frac{1}{2}$ and $S_z = -\frac{1}{2}$ for a single electron (positron) respectively. The singlet state is called para-positronium (p-Ps) and triplet state ortho-positronium (o-Ps). As a purely leptonic system properties of positronium can be determined solely via quantum electrodynamics.

3.1.1 Para-positronium

Due to charge conservation para-positronium decays into even numbers of photons, however probability quickly decreases with the number of photons - branching ratio for the decay into four photons is $1.439(2) \cdot 10^{-6}$ [43]. The decay rate of para-positronium was found to be [44, 45],:

$$\Gamma(\text{p-Ps} \to 2\gamma) = 7990.9 \cdot 10^6 s^{-1} \tag{3.2}$$

inverse of which gives mean lifetime of para-positronium in vaccum:

$$\tau_{\text{p-Ps}} = 125 ps. \tag{3.3}$$

3.1.2 Ortho-positronium

Ortho-positronium decays into odd number of photons with branching ratio for the decay into five photons of $[1.67 \pm 0.99 \pm 0.37] \cdot 10^{-6}$ [45, 46]. Decay rate of ortho-positronium is [45, 47]:

$$\Gamma(\text{o-Ps} \to 3\gamma) = 7.0404 \cdot 10^6 s^{-1} \tag{3.4}$$

inverse of which gives mean lifetime of ortho-positronium in vaccum:

$$\tau_{\text{o-Ps}} = 142ns \tag{3.5}$$

3.2 Quantum entanglement

Quantum entanglement is a physical phenomena that occurs when the state of a group of particles cannot be described independently by the state of individual particles even if they are separated spatially by a large distance. Mathematically, if the state of the two particle system $|\psi\rangle$ can be described as a product of state of each particle: $|\psi\rangle = |\phi_1\rangle\,|\phi_2\rangle$ the state is separable, otherwise it is entangled. In 1935 Einstein, Podolsky and Rosen [35], starting from three reasonable assumptions of locality, reality and completeness that every physical theory must satisfy, argued that quantum mechanics (QM) is an incomplete theory. They did not question quantum mechanics predictions but rather quantum mechanics interpretation [48]. Their argument was based on some inconsistencies between quantum mechanics and their local-realistic premises (LR) which appear for quantum states of bipartite systems, $|\psi\rangle \in \mathcal{H}_{d_1} \otimes \mathcal{H}_{d_1}$. In 1964, Bell showed that any theory compatible with LR assumptions can not reproduce some of the statistical predictions of QM [49], in his derivation, quantum correlations or entanglement have a crucial role. The conflict between local realism and quantum mechanics arises since the latter violates some experimentally verifiable inequalities, called Bell inequalities, that any theory according to the local-realistic assumptions should to satisfy. It is then possible to design real experiments testing QM against LR [50]. Correlations of linear polarizations of pair of photons were measured in 1982 showing strong agreement with quantum mechanichs predictions and violating Bell inequalities [51]. Nowadays, Bell inequalities have been tested thoroughly in favor of quantum mechanics [52].

3.2.1 Entanglement in p-Ps decay

The description of the two-photon state coming from the p-Ps decay is simply given by the lowest order Feynmann diagram of $e^+e^- \to \gamma\gamma$ (see [53] for details). Positronium is a non-relativistic particle to a very good approximation, this implies that the tree-level calculation of the annihilation of p-Ps into two photons is equal to, up to constants,

$$\mathcal{M}(e^+e^- \to \gamma\gamma) \sim \chi_+^{c\dagger} M_2 \chi_-, \tag{3.6}$$

where $\chi_\pm$ is the two component spinor describing the fermions, $\chi^{c\dagger} = \chi_T i\sigma_2$ and M_2 gives:

$$M_2 = \sum_{perm} (\vec{\epsilon_1}^* \times \vec{\epsilon_2}^*) \cdot \hat{k} I_{2x2} \equiv A(\hat{k}_1, \lambda_1; \hat{k}_2, \lambda_2) I_{2x2}, \tag{3.7}$$

where $\epsilon_1^* \equiv \epsilon^*(\hat{k}_1, \lambda_1)$ is the circular polarization vector associated with the outgoing photon i and I_{2x2} is identity matrix. To be more precise, for a photon having the

three-momentum vector $\vec{k} = \left|\vec{k}\right|\hat{k} = \left|\vec{k}\right|(\sin\theta\cos\phi, \sin\theta\sin\phi, \cos\theta)$ it's polarization can be chosen as:

$$\epsilon^*(\hat{k}, \lambda) = -\frac{\lambda}{\sqrt{2}}(\cos\theta\cos\phi - i\lambda\sin\phi, \cos\theta\sin\phi + i\lambda\cos\phi, -\sin\theta), \tag{3.8}$$

where $\lambda = \pm 1$ and they obey following rules:

$$\begin{aligned} \hat{k}\cdot\vec{\epsilon}(\hat{k},\lambda) &= 0 \\ \hat{k}\times\vec{\epsilon}(\hat{k},\lambda) &= -i\lambda\vec{\epsilon}(\hat{k},\lambda) \\ \vec{\epsilon}(\hat{k}_i,\lambda_i)\cdot\vec{\epsilon}(\hat{k}_j,\lambda_j) &= -\frac{1}{2}(1-\lambda_i\lambda_j\hat{k}_i\cdot\hat{k}_j). \end{aligned} \tag{3.9}$$

From the expressions of the polarizaton vectors and the three-momentum and energy conservation, scalar term A is

$$A(\hat{k},\lambda_1;-\hat{k},\lambda_2) = -\frac{i}{2}(\lambda_1+\lambda_2). \tag{3.10}$$

and it verifies

$$\begin{aligned} A(\hat{k},+1;-\hat{k},+1) &= A(\hat{k},-1;-\hat{k},-1) \\ A(\hat{k},+1;-\hat{k},-1) &= -A(\hat{k},+1;-\hat{k},-1) = 0. \end{aligned} \tag{3.11}$$

Two fermions in the para-positronium ground state are in a singlet state $|S=0, S_z=0\rangle = \frac{1}{\sqrt{2}}(|\uparrow\rangle|\downarrow\rangle - |\downarrow\rangle|\uparrow\rangle)$ and then, using previous relations for A and eq. 3.6 follows that the final state after annihilation is:

$$|\psi\rangle = \frac{1}{\sqrt{2}}(|{+}{+}\rangle - |{-}{-}\rangle) \tag{3.12}$$

where $|+\rangle$ and $|-\rangle$ denote left and right circular polarization of a photon. We can then describe this state in terms of linear photon polarization by substituting $|+\rangle = \frac{1}{\sqrt{2}}(i|H\rangle + |V\rangle)$ and $|-\rangle = \frac{1}{\sqrt{2}}(|H\rangle + i|V\rangle)$:

$$|\psi\rangle = \frac{1}{\sqrt{2}}(|HV\rangle + |VH\rangle) \tag{3.13}$$

where $|H\rangle$ and $|V\rangle$ stand for horizontal and vertical linear polarization. The two-photon state resulting from p-Ps decay is thus equivalent to a maximally entangled state of two spin-$\frac{1}{2}$ particles. This is a well-known result and was, actually, one of the physical system first proposed as a source of particles having the quantum correlations needed to test quantum mechanics vs local realism [54].

3.3 Klein-Nishina formula

One of the effects in which polarization of photons is manifested is Compton scattering where photon is scattered on a charged particle, usually electron. Such interaction is described by Klein-Nishina differential cross section [26]:

$$\begin{aligned}\frac{d\sigma(E,\theta,\eta)}{d\Omega} &= \frac{r_0^2}{2}\left(\frac{E'}{E}\right)^2\left(\frac{E}{E'}+\frac{E'}{E}-2\sin^2\theta\cos^2\eta\right)\\ &= \frac{r_0^2}{2}\left(\frac{E'}{E}\right)^2\left(\frac{E}{E'}+\frac{E'}{E}-\sin^2\theta\right)\{1-\mathcal{V}(\theta,E)\cos(2\eta)\}\end{aligned} \tag{3.14}$$

with

$$E'(E,\theta) = \frac{E}{1+\frac{E}{m_e c^2}(1-\cos\theta)}\,, \tag{3.15}$$

$$\mathcal{V}(\theta,E) = \frac{\sin^2\theta}{\frac{E}{E'}+\frac{E'}{E}-\sin^2\theta} \tag{3.16}$$

where r_0 is classical electron radius, E is the energy of initial photon, E' is the energy of photon after scattering, θ is the Compton scattering angle and η is the angle between scattering and polarization planes (fig. 1.1). The expression $\mathcal{V}(\theta,E)$ quantifies the interference contrast, called visibility. If the visibility is close to zero, the oscillation due to the polarization degree of freedom are not observable. In this case no information on the polarization degree of freedom can be deduced. For $511keV$ photons the maximum of the visibility is obtained for a scattering angle of $\theta = 81.67°$ and the minimum of the visibility is obtained for both small and large scattering angles θ, independently of the photon's energy.

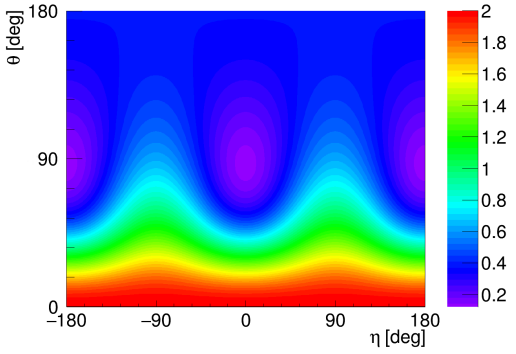

(a) Klein-Nishina differential cross section (eq. 3.14) for photons with initial energy $E = 511keV$ shown as a function of θ and η angles.

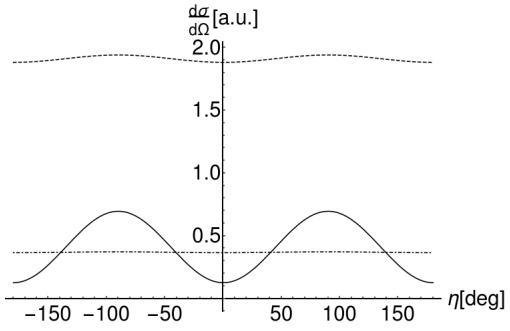

(b) Klein-Nishina differential cross section (3.14) for photons with initial energy $E = 511keV$ presented as a function of angle η. Dashed, solid, and dot-and-dashed lines shows results for scattering at angles $\theta = 10°$, $\theta = 81.67°$, and $\theta = 170°$, respectively.

Figure 3.1: Klein-Nishina differential cross section for photons with initial energy $E = 511keV$.

The figure 3.1a shows the calculated differential cross section for Compton scattering of $511keV$ photons, as a function of η and θ angles (eq 3.14). As

expected, for θ around $82°$ a most pronounced modulation of the cross section as a function of the η angle is observed. The amplitude of modulations decreases towards higher and lower values of θ. A quantitative comparison of this dependence is shown for three chosen angles in the left panel of Fig. 3.1b.

3.4 Joint cross section

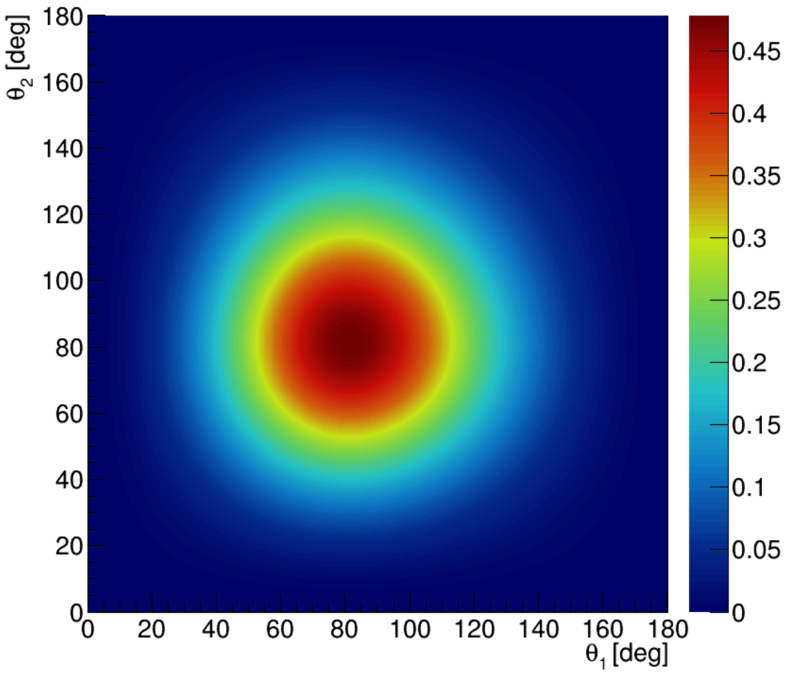

Figure 3.2: Visibility in double photon Compton scattering. Value of this function determines interference contrast of the angle between scattering planes. This contrast is highest when both photons scatter at Compton angle $\theta = 81.67°$ and tends to zero for very small and very big Compton scattering angles.

Klein-Nishina formula can be rewritten in Kraus operator representation [4]:

$$\sigma_\rho = \frac{r_0}{2}\left(\frac{E'}{E}\right)^2 \left\{\mathrm{Tr}\left(\mathcal{K}_1\,\rho\,\mathcal{K}_1^\dagger\right) + \mathrm{Tr}\left(\mathcal{K}_2\,\rho\,\mathcal{K}_2^\dagger\right)\right\} \tag{3.17}$$

where ρ is a density matrix, σ_ρ is a differential cross section for a state ρ, and $\mathcal{K}_1, \mathcal{K}_2$ are defined as follow:

$$\mathcal{K}_1 = \sqrt{\left(\frac{E}{E'} + \frac{E'}{E} - 2\right)} \cdot \mathbb{1}_2, \qquad \mathcal{K}_2 = \begin{pmatrix} \varepsilon_H'^* \cdot \varepsilon_H & \varepsilon_H'^* \cdot \varepsilon_V \\ \varepsilon_V'^* \cdot \varepsilon_H & \varepsilon_V'^* \cdot \varepsilon_V \end{pmatrix} \tag{3.18}$$

where $\mathcal{K}_2$ describe transition amplitudes for polarization before and after scattering with respect to linear polarization basis. With such formulation we obtain an information theoretic form for any pure or mixed state. Additional advantage of this

representation is that it allows us straightforward generalization for system with any number of particles in any given state ρ:

$$\begin{gathered}\sigma_\rho = (\frac{r_0}{2})^z \left(\frac{k_a}{k_{i_a}}\right)^2 \left(\frac{k_b}{k_{i_b}}\right)^2 \cdots \left(\frac{k_z}{k_{i_z}}\right)^2 \cdot \\ \sum_{l_a,l_b,\ldots l_z=1}^{2} \mathrm{Tr}\left(\mathcal{K}_{l_a}^{(a)} \otimes \mathcal{K}_{l_b}^{(b)} \cdots \otimes \mathcal{K}_{l_z}^{(z)} \, \rho \, \mathcal{K}_{l_a}^{(a)\dagger} \otimes \mathcal{K}_{l_b}^{(b)\dagger} \cdots \otimes \mathcal{K}_{l_z}^{(z)^\dagger}\right)\end{gathered} \tag{3.19}$$

where z is a number of particles and $\mathcal{K}_{l_i}$ describes first and second Kraus operator for i-th particle. Considering two cases: 1) entangled state $|\psi_1\rangle = \frac{1}{\sqrt{2}}(|HV\rangle + |VH\rangle)$ and 2) separable state $|\psi_2\rangle = |HV\rangle$ and substituting corresponding density matrices to eq 3.19 we obtain [3]:

$$\sigma_{\rho_1} = r_0^2 \mathcal{F}(E_1,\theta_1)\mathcal{F}(E_2,\theta_2) \cdot \frac{1}{4}\left\{1 - \mathcal{V}(E_1,\theta_1)\mathcal{V}(E_2,\theta_2)\cos 2\varphi\right\} \tag{3.20}$$

$$\sigma_{\rho_2} = r_0^2 \mathcal{F}(E_1,\theta_1)\mathcal{F}(E_2,\theta_2) \cdot \frac{1}{4}\left\{1 - \frac{1}{2}\mathcal{V}(E_1,\theta_1)\mathcal{V}(E_2,\theta_2)\cos 2\varphi\right\} \tag{3.21}$$

where E_i and θ_i describe initial energy and Compton scattering angle of i-th particle, φ is an angle between scattering planes (see fig. 1.2) and $\mathcal{F}(E,\theta)$ is an envelope function defined as:

$$\mathcal{F}(E,\theta) = \left(\frac{E'}{E}\right)^2 \left(\frac{E}{E'} + \frac{E'}{E} - \sin^2\theta\right). \tag{3.22}$$

3.5 Areas of interest and expected distributions.

To compare measured distributions of the angle between scattering planes we need to calculate expected distributions based on equations 3.20 for entangled state and 3.21 for separable one. J-PET detector offers high geometrical acceptance for Compton scattering angles therefore we will calculate the distributions of certain ranges of Compton scattering angles.

We are interested in the distribution of the angle between scattering planes in few different ranges:

$$\begin{aligned}&\forall\theta_1,\theta_2 : \theta_1,\theta_2 \in [0,180]^\circ \\ &\forall\theta_1,\theta_2 : (\theta_1 - 82^\circ)^2 + (\theta_2 - 82^\circ)^2 < (30^\circ)^2 \\ &\forall\theta_1,\theta_2 : (\theta_1 - 100^\circ)^2 + (\theta_2 - 100^\circ)^2 < (30^\circ)^2 \\ &\forall\theta_1,\theta_2 : (\theta_1 - 92^\circ)^2 + (\theta_2 - 92^\circ)^2 < (10^\circ)^2\end{aligned} \tag{3.23}$$

Those ranges corresponds to four different areas: all measured events; as well as those that were inside three different circles shown on the visibility in double photon Compton scattering plot (Fig. 3.3) - one around point $(82^\circ, 82^\circ)$ with radius of 30° which is centered around the point of maximum visibility in order to maximize

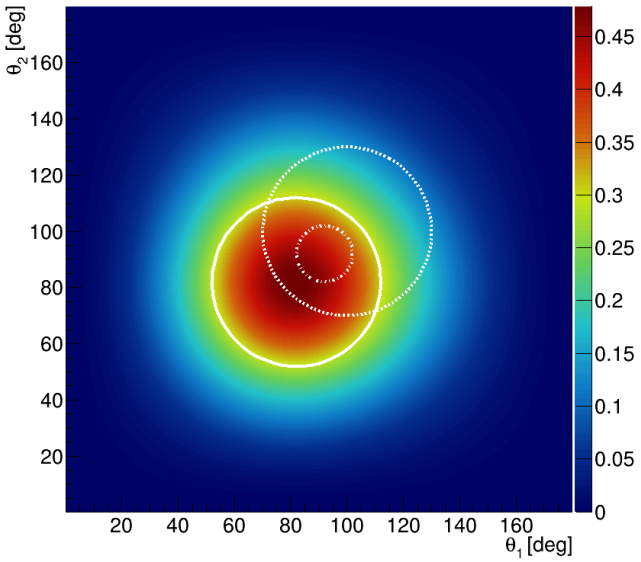

Figure 3.3: Areas of interest on visibility plot. We have chosen four different areas in which we will search for angle between scattering planes - one for all measured events and those within three circle - one around point of highest visibility (white solid circle) and two to maximise number of measured events (white dotted lines).

interference contrast, one around $(92°, 92°)$ with radius of $10°$ and one around point $(100°, 100°)$ with radius of $30°$ - last two circles were chosen to maximize the number of measured events (which will be described in section 4.1).
Distributions for both hypotheses can be found in fig. 3.4 where blue line represents result for separable state and green one for entangled. These are the distributions of the angle between scattering planes calculated as an average over the whole range (in one of the four described areas) and then normalized.

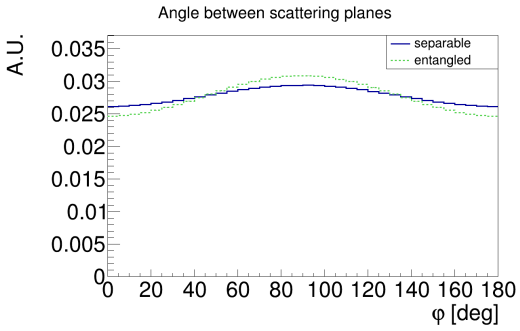

(a) Angle between scattering planes for all measured events.

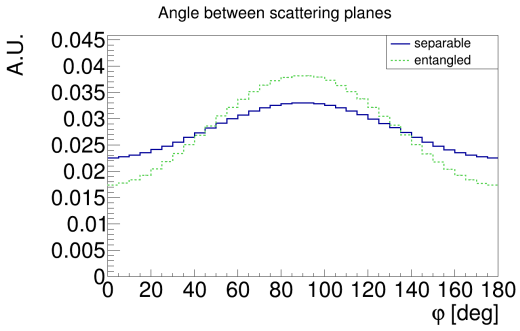

(b) Angle between scattering planes for events in circle around $(82°, 82°)$ with radius of $30°$.

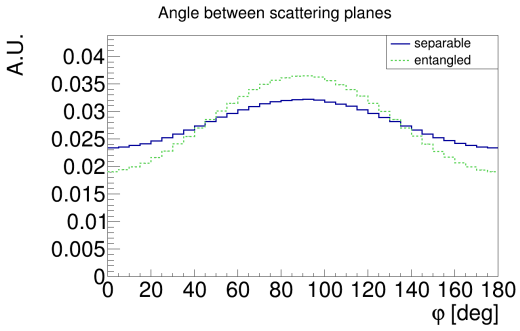

(c) Angle between scattering planes for events in circle around $(100°, 100°)$ with radius of $30°$

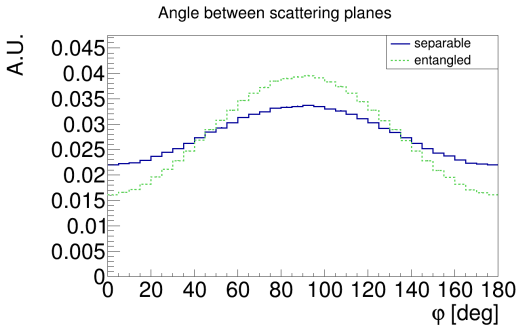

(d) Angle between scattering planes for events in circle around $(92°, 92°)$ with radius of. $10°$

Figure 3.4: Angle between scattering planes for events in four different area of interest. Results for two hypotheses are presented - that the photons from para-positronium annihilation are entangled (green dotted line) and that they are separable (blue solid line).

Experimental setup

4

4.1 Sodium as a source of positrons

Radioactive sodium ^{22}Na was used in the experiment as a source of positrons. Sodium undergoes β^+ decays:

$$^{22}Na \rightarrow {}^{22}Ne + e^+ + \nu + \gamma(1.27MeV) \tag{4.1}$$

where it decays into excited neon which then emmits deexcitation gamma quanta with the energy of 1.27MeV [55, 56]. When produced positrons are implanted in materials, they rapidly lose kinetic energy in a variety of interactions (bremsstrahlung, ionization, electron excitation, phonon excitation, vibrational and rotational excitation, positronium formation, etc.) approaching the thermal energy [57, 58].

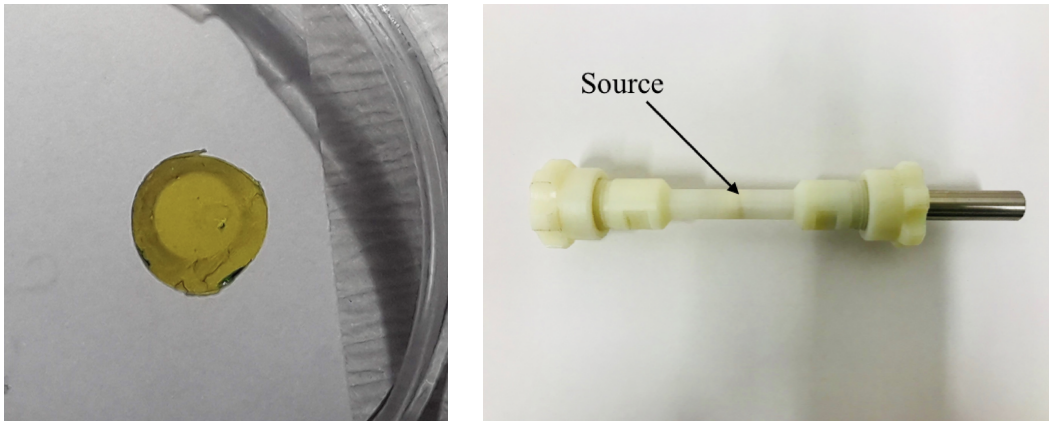

(a) Sodium ^{22}Na source sandwiched between two sheets of kapton foil. Such prepared source was then placed between XAD4 material and placed inside plastic annihilation chamber (fig 4.1b).

(b) Photo of plastic annihilation chamber. Annihilation chamber is made of polyamide PA4 which low density ($1.14\frac{g}{cm^3}$) provides low attenuation of gamma particles originating from positronia annihilations [59]. Sodium source was placed in the center of the chamber which was then placed in the center of the J-PET detector (fig. 4.2c).

Figure 4.1: Annihilation chamber with sodium source used in the measurement.

In the experiment sodium source was placed between two thin sheets of kapton foil which was then placed between XAD4 material. XAD4 is a polymer with relatively large pores inside it (average pore size of about 100Å) which increases the amount of created ortho-positronia inside it. Such polymer-sandwich was then placed inside plastic annihilation chamber made of polyamide PA6 of density $1.14\frac{g}{cm^3}$ which was chosen due to it's low attenuation of gamma particles from positronia annihilations [59].

4.2 J-PET detector

The Jagiellonian Positron Emission Tomograph (J-PET) is a device that was build with medical application in mind as a cost-effective scanner for simultaneous

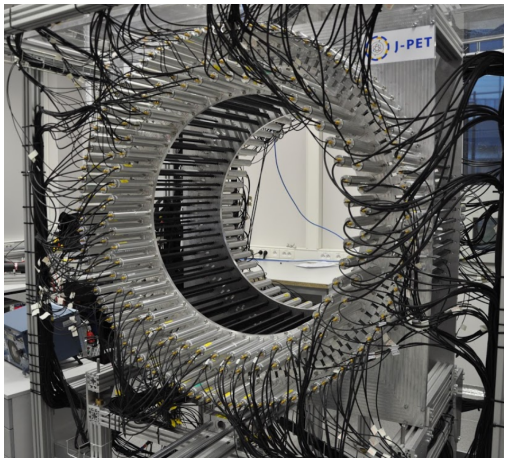

(a) Photo of the detector. Black strips are the scintillators wrapped in light protective foil. On both sides of the scintillators there are silver tubes which are the housings of photomultipliers. Each photomultiplier is connected to the power supply and the readout electronics by the black cables.

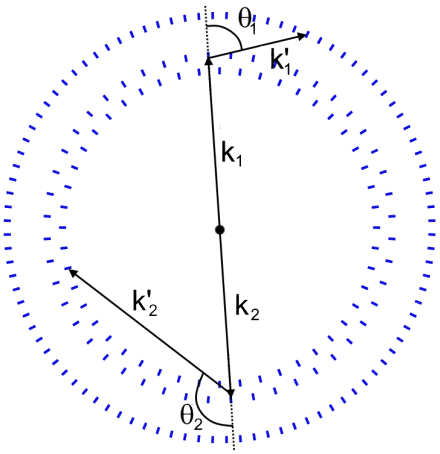

(b) Schema of back-to-back momenta from e^+e^- annihilations. Primary photons with momenta k_1 and k_2 are scattered inside scintillators with Compton scattering angles of θ_1 and θ_2 where they are registered, then both scattered photons (with momenta k_1' and k_2') are registered again allowing the reconstruction of the angle between scattering planes (see Fig. 1.2).

(c) Annihilation chamber (fig. 4.1) placed in the center of the detector. This chamber was attached to two metal rods which were then placed on a movable plastic holders. Such setup allowed to fine-tune the position of the source to be in the center of the detector.

Figure 4.2: Detection setup used for the experiment described in this thesis.

metabolic imaging of the whole human body [60, 61], and positronium imaging [17] however it's unique design provides opportunities for studies of fundamental physical phenomena such as discrete symmetries and quantum entanglement [1, 24, 62, 63, 55]. Main idea behind J-PET scanner was to use plastic scintillators instead of scintillating crystals [64, 19]. PET scanners currently offered on a market are using crystals due to their high detection efficiency and energetic resolution [65]. Plastic scintillators are easily manufactured and can be molded into any desired shape or length while being at least an order of magnitude cheaper than crystals at the same time offering superior time resolution and light attenuation length around ten times higher than crystal scintillators. Those features enable creation of a few meters long detectors resulting in higher field of view (FOV) than currently sold scanners, as well as enable usage of the time of flight (TOF) technique which improves resolution of tomographic images. In this design light is registered by two photomultipliers, one at each end of scintillating strip [66, 15], in contrast to other PET scanners where photomultipliers point towards the center of the detector and are placed along whole length of the scintillating crystals. Such design results in a much less complex readout system as well as enables usage of additional detection layers, which leads to increased detection efficiency therefore suppressing main disadvantage of plastic scintillators [14].

Current iteration of the J-PET detector is made out of 192 EJ-230 plastic scintillators arranged concentrically in three layers around the Z axis of the detector. Diameters of those layers are: $850mm$, $953mm$ and $1150mm$ and they consist of 48, 48 and 96 scintillators respectively [19]. Each scintillator have a dimentions of $7 \times 19 \times 500mm^3$ and light signals are registered at both ends by Hamamatsu R9800 vacuum tube photomultipliers (PMT) and converted to electrical signals [19]. Those signals are then probed at four differend threshold values in the voltage domain with accuracy of around $30ps$ by multi-constant-threshold boards combined with Trigger Readout Board v3 hardware equipped with Time-to-Digital Converters (TDC) [20] and Field Programmable Gate Array devices resulting in 8 points (4 at the leading and 4 at trailing edge of the signal) from which whole signal can be reconstructed [67].

4.2.1 Position of interaction and energy deposition

Due to a unique design where long scintillator strips were used, in order to determine position of the interaction we are measuring time at which light reached photomultiplier on both sides of scintillator (let's call them A and B). Distance between point of interaction (Δl) and center of the scintillator is given by:

$$\Delta l = \frac{(t_B - t_A)v}{2} \tag{4.2}$$

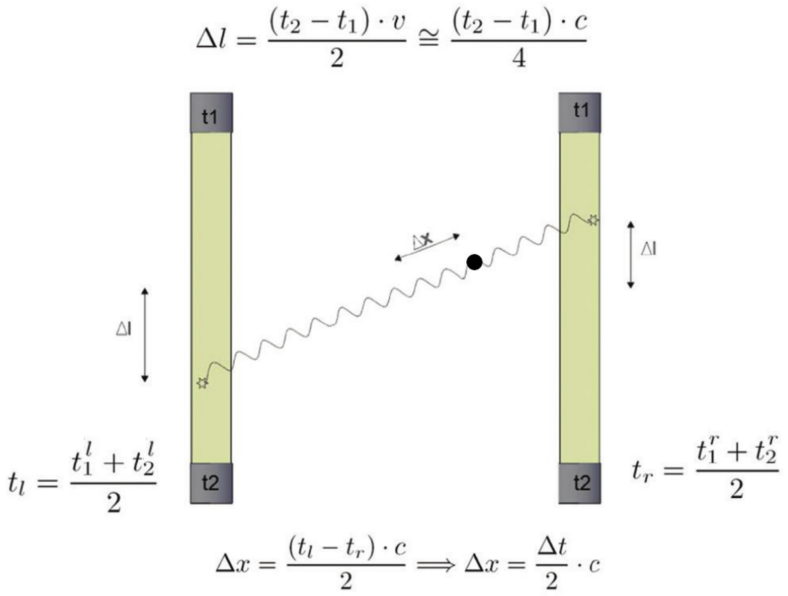

(a) Determination of the position and time of interaction. Each scintillator measures time at which signal from the scintillator arrived at it, those being t_1^l, t_2^l, t_1^r and t_2^r. Position of the interaction can be calculated with those times as the offset from the center $\Delta l = \frac{(t_2-t_1)v}{2} \approx \frac{(t_2-t_1)c}{4}$. Time of interaction in a scintillator can be calculated as $t = \frac{t_1+t_2}{2} - \frac{L}{c}$, where L is the length of the scintillator. Image taken from [68]

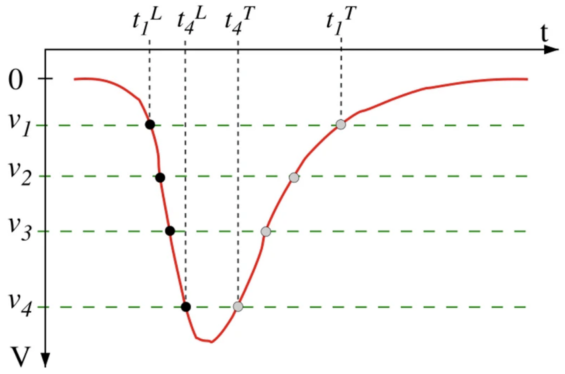

(b) Time over threshold (TOT) method used to estimate energy deposited in the scintillator. Signals from photomiltipliers were probed on four different experimental voltage thresholds v_i on both leading and trailing edge and time at which signal passed specific threshold were registered (t_i^L on leading and t_i^T on trailing edge respectively). TOT was then calculated as eq. 4.5 and used to estimate energy deposited during the Compton scattering.

Figure 4.3: Methods to determine time and position of interaction and estimate deposited energy.

where v is effective velocity of light propagating in the scintillating strip and it's equal to $12.61 \pm 0.05_{stat} \pm 0.01_{sys} \frac{cm}{ns}$ [12]. Time of this interaction can be reconstructed as:

$$t = \frac{t_A + t_B}{2} - \frac{L}{c}, \tag{4.3}$$

where L is the length of the scintillator.

If there was back-to-back decay and both photons were registered, a point of annihilation can be reconstructed in a similar way, that is the distance of annihilation point from the center of the line of response (Δx) is given by:

$$\Delta x = \frac{(t_1 - t_2)c}{2} \tag{4.4}$$

where t_1 and t_2 are times of interaction in first and second scintillator.

In a J-PET detector a direct measurement of charge generated at a photomultiplier is not applied in order to avoid long time such measurement requires. Instead a time at which signal crossed specific threshold is measured at both leading and trailing edge. Such measurement is much faster and due to a fact that every signal is measured at four different thresholds allowing for an estimation of the charge of the signal. This technique is called Time Over Threshold (TOT) and works as follows: time in which signal was above specific threshold is measured and multiplied by the difference between this and previous threshold level (fig. 4.3b). It can be expressed by an equation:

$$\begin{aligned} TOT = &\frac{Thr_1 - Thr_0}{Thr_4 - Thr_3} TOT_1 + \frac{Thr_2 - Thr_1}{Thr_4 - Thr_3} TOT_2 + \\ &\frac{Thr_3 - Thr_2}{Thr_4 - Thr_3} TOT_3 + \frac{Thr_3 - Thr_4}{Thr_4 - Thr_3} TOT_4 \end{aligned} \tag{4.5}$$

where TOT_i is time over i-th threshold, Thr_i is the value of i-th threshold in mV where Thr_0 is the base level of $0mV$. Whole Time Over Threshold is normalized by the difference between two last thresholds, so when thresolds levels are uniformly distributed whole TOT is just a sum of times over all four thresholds.

4.3 Software for MC simulations and data analysis

4.3.1 J-PET Framework

Data measured by the J-PET detector are analyzed by the dedicated software developed by the J-PET group called J-PET Framework [23]. It is an open-source platform for data analysis which provides environment for calibration and data filtration procedures, image reconstruction as well as specific user-defined analysis procedures. The library is written using C++ language. It's based on ROOT package and contains set of building blocks that can be combined even by users with little to no programming experience and can handle multiple different inputs such as: low-level data from the detector acquisition system or an oscilloscope, high-level tomography structures like lines-of-response or results from Monte Carlo simulations using packages like Geant4 [69] or GATE [70].

4.3.2 Geant4

In order to asses detector response to the physical phenomena J-PET group developed Monte Carlo simulation package, based on Geant4, which controls tracking particles through the detector. Developed software allows simulation of direct e^+e^- annihilation as well as formation of ortho- and para-positronium and pick-off process. It also supports simulation of any detector part based on Computer Aided Design (CAD), such as metal frame holding scintillators.

4.4 Conducted measurement

Sodium source with activity of 1MBq was placed inside of an annihilation chamber (described in chapter 4.1) which was connected to a vaccum system (via metal rod in Fig. 4.2c) and constant pressure of 1.2Pa was insured inside the annihilation chamber. Continuous measurement of positronia decays in a trigger-less mode was performed between 29th August and 8th of November 2019. In total 45TB of data were collected and analyzed.

5 Monte Carlo simulations of the experimental setup and expected results

In order to compare experimental results with theoretical predictions the influence of detector geometry, it's detection efficiency and precision as well as influence of the chosen selection criteria on the measured data had to be studied. It was done by detailed Monte Carlo simulations of the detection setup.

Figure 5.1 describes quantities measured in the experiment. We are measuring time t_i and position $\vec{x_i} = (x_i, y_i, z_i)$ of photons interaction. We are also calculating distances between secondary photon interaction point and both primary photons interactions point denoted as $d_{1/2}$ for first and second primary photon respectively, which will be later used to classify whether the photon scattered from first or second primary.

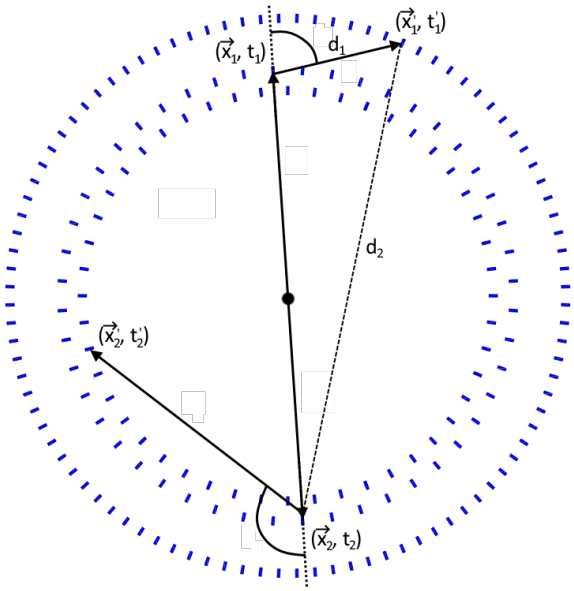

Figure 5.1: Schematic of values measured in the experiment. We are able to reconstruct times (t) and positions ($\vec{x} = (x, y, z)$) of interactions. We are also introducing variable $d_{1/2}$ which is a distance between scattered photon interaction point and first and second primary photons interaction points respectively.

5.1 Details of performed simulation

Monte Carlo simulation of the experimental setup was performed using dedicated software based on Geant4 (as described in 4.3.2). Inside the detector, build out of 192 scintillators arranged in three concentric cylinders annihilation chamber was placed. In order to make computations faster, sodium source, it's decay and

positronium forming is not simulated, instead it's assumed that positronium was formed in a porous material, in a random place within the effective range of positron that would come from decaying sodium source in the center of the detector (Fig. 5.2). Types of events that were simulated are: decays of p-Ps into two photons; decays of o-Ps into two photons due to pick-off process, direct e^+e^- annihilation as well as decays into three photons from direct annihilation and o-Ps. Every decay has an additional prompt gamma from sodium decay and lifetime depends on annihilating state and material in which annihilation took place. Decays of p-Ps into two photons have an additional assumption that it's state is $|\psi\rangle = |HV\rangle$ that is polarization of those photons are orthogonal.

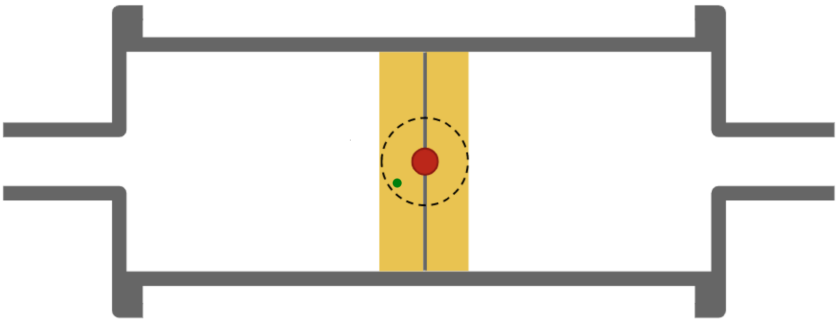

Figure 5.2: Schematic description of the annihilation chamber used in the simulations. Sodium source (red dot) was held in place with kapton foil and placed between porous material XAD4 (yellow). Positronium was formed within effective range of positron in this material and it's marked with green dotted-circle.

In total 10^{11} decays were simulated event-by-event and were merged using J-PET Framework software with the assumption that decaying source had activity of 1MBq which corresponds to 1 day 3 hours 46 minutes 40 seconds of "real time" measurement. Points of interactions were also smeared with a gaussian function assuming experimental resolution of [19]:

$$\begin{aligned} \sigma_Z &= 2.5cm \\ \sigma_t &= \frac{220ps}{\sqrt{E_{dep}/340keV}}, \\ \sigma_{E_{dep}} &= \frac{0.06 \cdot E_{dep}}{\sqrt{E_{dep}/1000keV}}. \end{aligned} \tag{5.1}$$

5.2 Selection criteria applied to simulated data

After applying smearing of the data, interaction points were arranged into events and analyzed using following selection criteria. Length of the scintillator is 50cm with coordinate system chosen such that center of the scintillator had coordinate $Z = 0$, and part of it is covered by photomultipliers and metal frame that holds detector together therefore it's assumed that photons could not interact at the ends

of scintillating strip (Fig. 5.3) therefore only those interactions which were between plus and minus 23cm from the center of the scintillator were kept for further analysis.

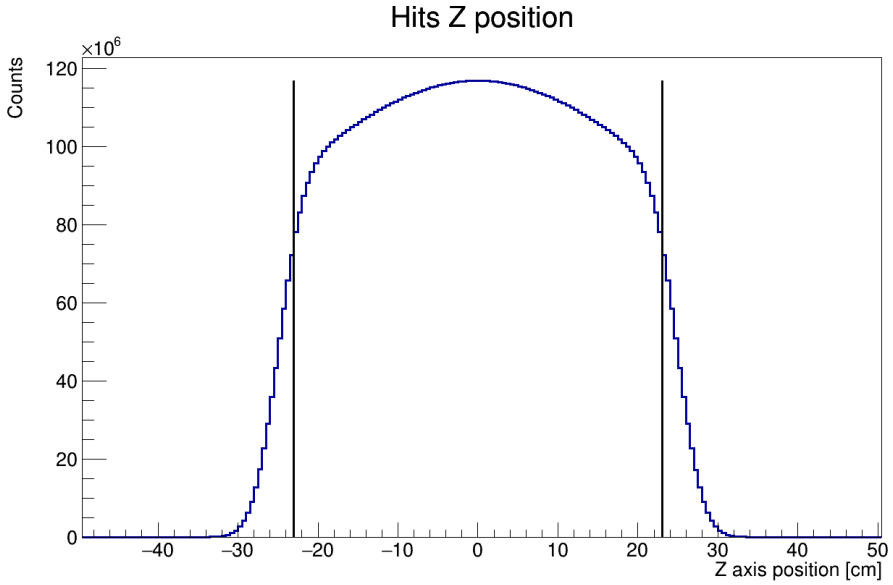

Figure 5.3: Z position of reconstructed interaction point. We are keeping for further analysis only those hits that were reconstructed in the active scintillator length, $|Z| <$ 23cm. Length of the scintillating strip was 50cm and ends of it were placed in metal frame to hold them in place. We are discarding events at the very ends of scintillating strip to remove any effects that could come from accidental scatterings in the frame.

Next step was to select subset of the data that could come from annihilation based on the deposited energy: if energy deposition was in range of $30keV < E_{dep} < 340keV$ interaction was tagged as annihilation and analyzed further. Lower bound of this range corresponds to the lowest voltage threshold set on the data acquisition system and upper one is the maximal energy that photon of initial energy of $511keV$ can deposit in Compton scattering (Fig. 5.4). Those two conditions removed from the sample hits that could not come from o-Ps decay due to too high energy deposition and interaction outside of the active scintillation length and only events that contained exactly four hits after those cuts were subjected to the further analysis.

Next step was to find two photons coming from back-to-back decay. Since they are coming from the same annihilation they must have been emitted at the same time. Let's introduce two different times: t which is time of interaction and $\tau = t - \frac{d}{c}$ which is time of emission defined as time of interaction reduced by the time of flight (d is the distance between points of annihilation and interaction). For every pair of hits that fulfilled previous conditions we are checking difference between those two times (Fig. 5.5) and assuming it could have been back-to-back hits if $|\tau_i - \tau_j| < 500ps$. For every pair of hits that passed this condition the position of annihilation point on the XY plane was calculated (Fig. 5.6) and if the position was within 1cm from the center of the detector also Z position of the annihilation point

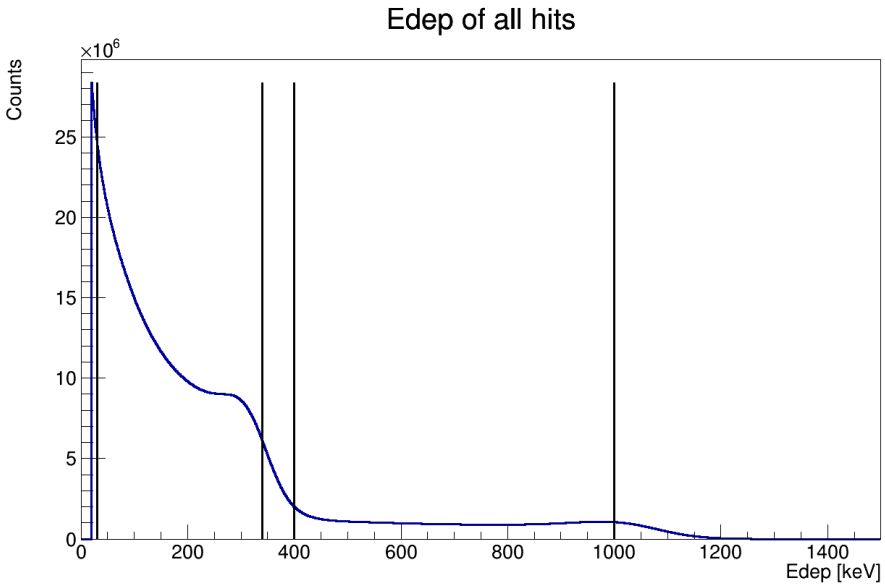

Figure 5.4: Reconstructed energy deposited in the scintillator. If reconstructed energy distribution is within range $30keV < E_{dep} < 340keV$ such hits are tagged as coming from positronium annihilation and analyzed further. We are interested only in photons coming from annihilation therefore having energy of $511keV$ (for the primary photons). Maximum energy deposition for such photons is $340keV$ for scattering at $\theta = 180°$ and lower bound value of $30keV$ was chosen to mimic lowest experimental thresold.

was calculated (Fig. 5.8). If that position is within $-4cm < Z < 4cm$, and only one pair of hits fulfilled all those conditions it's assumed to be a back-to-back pair.

After successful finding of the back-to-back pair we need to assign scattered hits to corresponding primary hits. In order to do so we are introducing a parameter Δ_i:

$$\Delta_{1/2} = \left| t_{1/2} - t' \right| - \frac{d_{1/2}}{c} \tag{5.2}$$

where $t_{1/2}$ is time of interaction of first or second primary photon, t' is time of interaction of scattered photon and $d_{1/2}$ is distance between scattered photon and first or second primary photon. This parameters compares time it would took to photon to travel from point of primary interaction ($\frac{d}{c}$) with time difference between two interactions ($|t - t'|$). In the case of perfect measurement this parameter should be equal to zero if scattering comes from the primary interaction and it should be different from zero when it did not. To select correct scattering we are creating plot of Δ_1 vs Δ_2 and introduce elliptical cuts to assign scattering to first or second primary interaction. Equation defining ellipse is as follows:

$$\frac{((x - x_0)\cos\alpha + (y - y_0)\sin\alpha)^2}{a^2} + \frac{((x - x_0)\sin\alpha - (y - y_0)\cos\alpha)^2}{b^2} = 1 \tag{5.3}$$

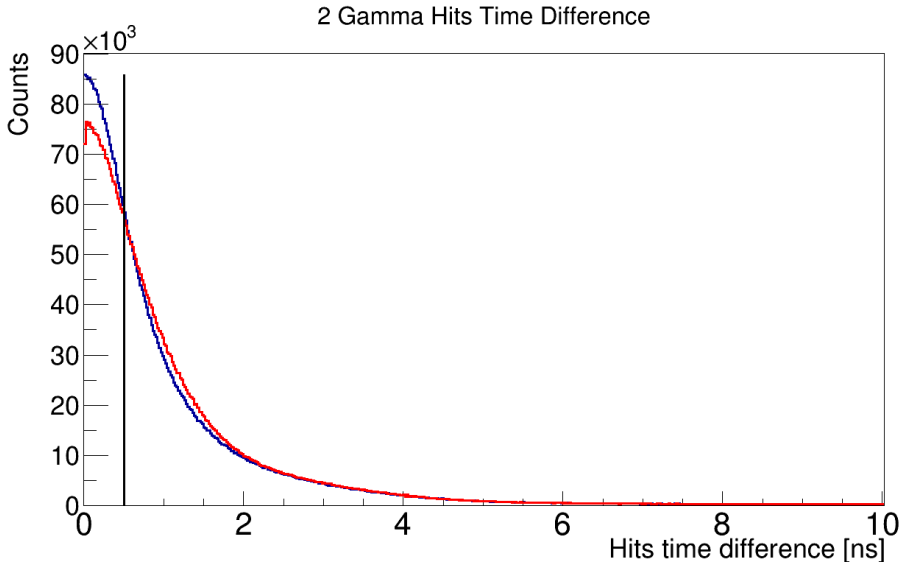

(a) Full spectrum of time difference between two hits.

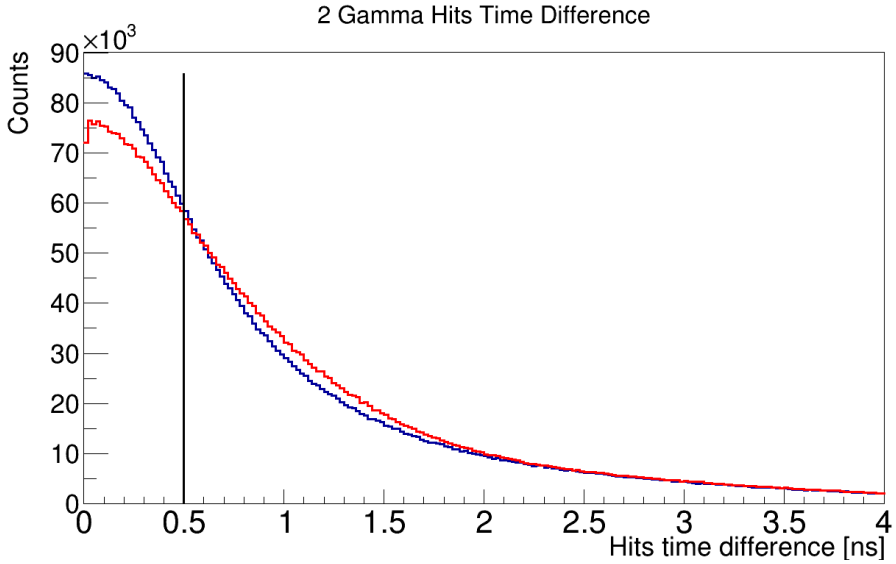

(b) Spectrum of time difference between two hits zoomed into an area of interest.

Figure 5.5: Time difference between every pair of hits. We are checking both time of interaction (blue line) and time of emission (red line) for each pair of hits within an event. If the time difference of interaction is lower than $500ps$ we are assuming that such pair can come from back-to-back decay therefore analyzing it further.

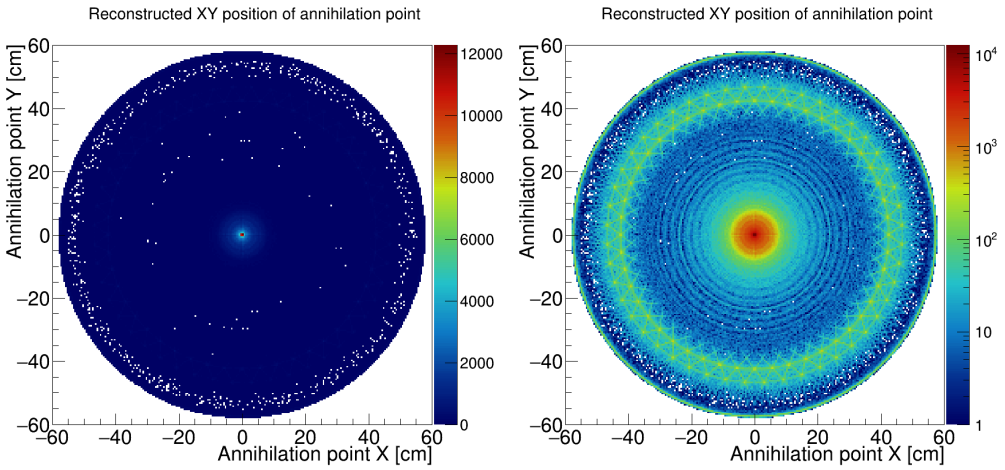

(a) Linear scale. **(b)** Logarithmic scale.

Figure 5.6: Reconstructed XY position of annihilation point. For every pair of hits that fulfilled previous conditions (that is position of interaction and time difference between interactions) position of annihilation point on the XY plane was calculated.

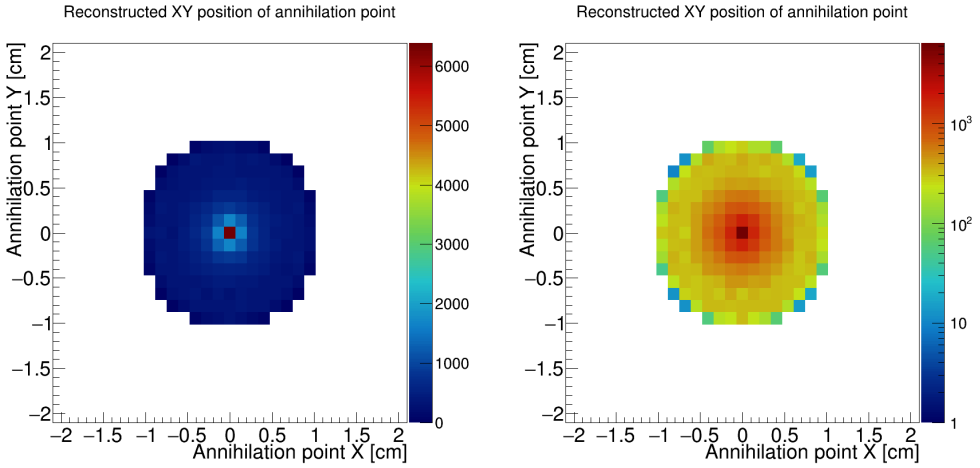

(a) Linear scale. **(b)** Logarithmic scale.

Figure 5.7: Selected annihilation points. If reconstructed XY position of annihilation point was closer than $1cm$ from the center of the detector we are assuming it came from back-to-back decay and analyze such pair further.

where x_0 and y_0 define center of an ellipse, a and b are semi-axis in X and Y direction respectively and α is the angle measured from X axis. Parameters of ellipses used in cuts in this selection can be found in table 5.1.

If Δ_1 and Δ_2 parameters are in lower-right ellipse scattering is assumed to come from first primary photon; if they are in upper-left ellipse it's assumed to come from second photon. After this selection procedure if exactly one photon was labeled as scattered from first primary and exactly one photon as scattered from second primary then all four interactions were found and distribution of Compton scattering angles as well as angle between scattering planes can be created (Fig. 5.10).

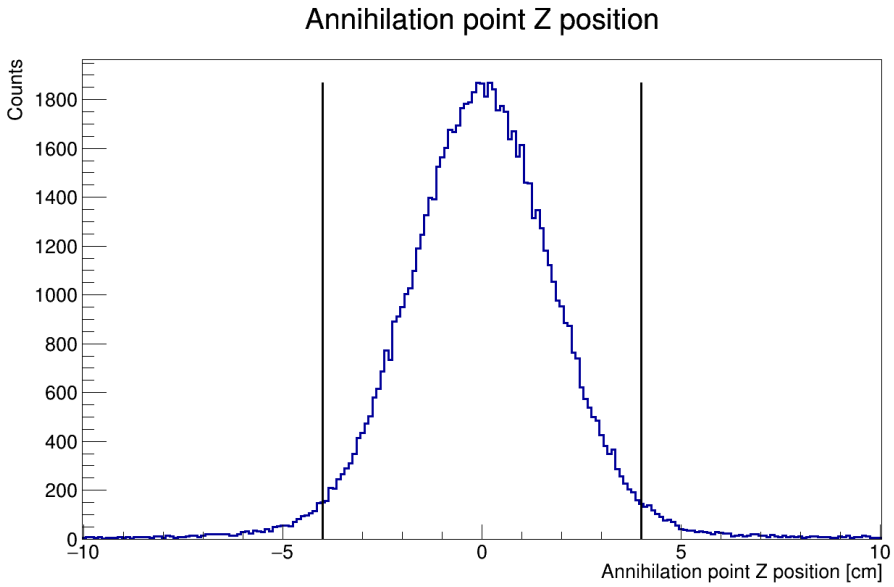

Figure 5.8: Reconstructed Z position of annihilation point. We are assuming that pair of hits came from back-to-back decay if $|Z| < 4cm$.

Parameter	Upper left	Lower right
x_0	-2.31 ns	0.45 ns
y_0	0.48 ns	-2.43 ns
a	1.7 ns	1.7 ns
b	0.7 ns	0.7 ns
α	30 deg	60 deg

Table 5.1: Parameter of ellipses (eq. 5.3) used for cuts in scattering test.

5.3 Simulation of quantum entanglement of two photons

In order to compare experimental results against two hypotheses: that the state of photons after a decay is entangled and that it's separable we need to generate detector response for the entangles state. To do that we introduce following function Λ:

$$\Lambda(\theta_1, \theta_2, \varphi) = \frac{1 - \mathcal{V}(\theta_1)\mathcal{V}(\theta_2)\cos 2\varphi}{1 - \frac{1}{2}\mathcal{V}(\theta_1)\mathcal{V}(\theta_2)\cos 2\varphi} \tag{5.4}$$

$$\Lambda_{max}(\theta_1, \theta_2) = \frac{1 + \mathcal{V}(\theta_1)\mathcal{V}(\theta_2)}{1 + \frac{1}{2}\mathcal{V}(\theta_1)\mathcal{V}(\theta_2)} \tag{5.5}$$

which is eq. 3.20 divided by eq. 3.21. Oscillation amplitude is two times higher for entangled state, therefore in order to generate spectrum for entangled state (increase oscillation amplitude) we need to discard some events. Procedure to do that is as follows: for every reconstructed event in Monte Carlo we can calculate θ_1, θ_2 and φ and then calculate the ratio function $\Lambda(\theta_1, \theta_2, \varphi)$. We also calculate $\Lambda_{max}(\theta_1, \theta_2)$ and

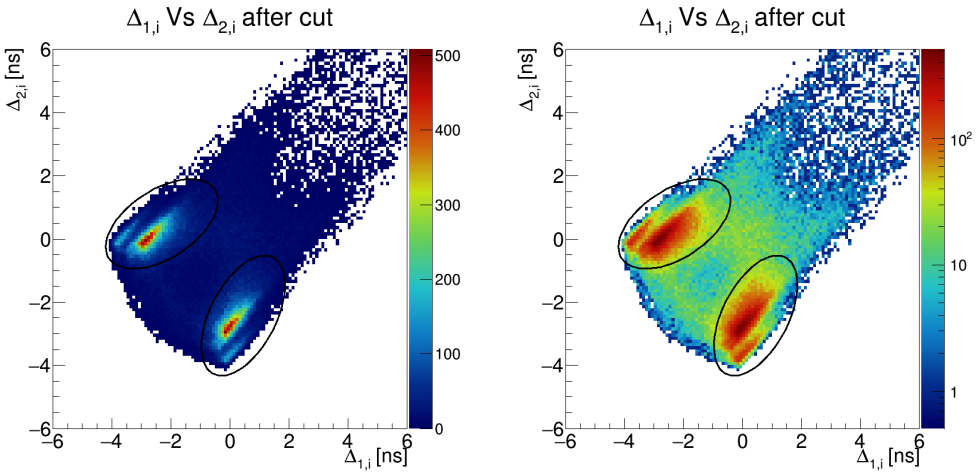

(a) Linear scale. **(b)** Logarithmic scale.

Figure 5.9: Scatter test. After identifying both primary photons we need to assign scattered photons to the correct primary ones. It was done by calculating parameter Δ (see eq. 5.2). This parameters compares time it would took to photon to travel from point of primary interaction with time difference between two interactions. In the case of perfect measurement this parameter should be equal to zero if scattering comes from the primary interaction and different than zero when it did not (however wee need to account for experimental precision). To select correct scattering we are creating plot of Δ_1 vs Δ_2 and introduce elliptical cuts to assign scattering to first or second primary interaction (parameters of the ellipses can be found in table 5.1)

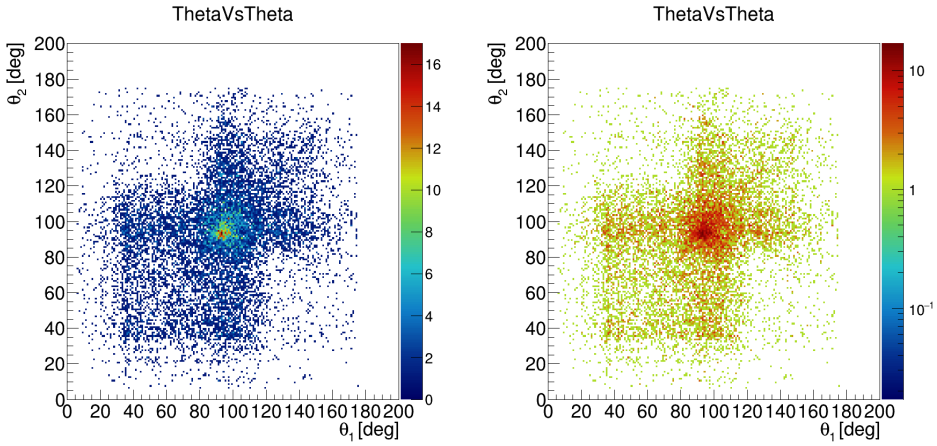

(a) Linear scale. **(b)** Logarithmic scale.

Figure 5.10: Reconstructed Compton scattering angles. After positively identifying both primary photons and assigning both scattered photons to their corresponding primary ones we are able to calculate Compton scattering angles.

generate random number $x \in U[0, \Lambda_{max}]$ from uniform distribution between 0 and Λ_{max}. Next step is to compare value of randomly generated number x with value of ratio function at reconstructed angle between scattering planes $\Lambda(\theta_1, \theta_2, \varphi)$ and if it's smaller we keep the event and assume it's entangled. Graphical representation of this method can be found in Fig. 5.11.

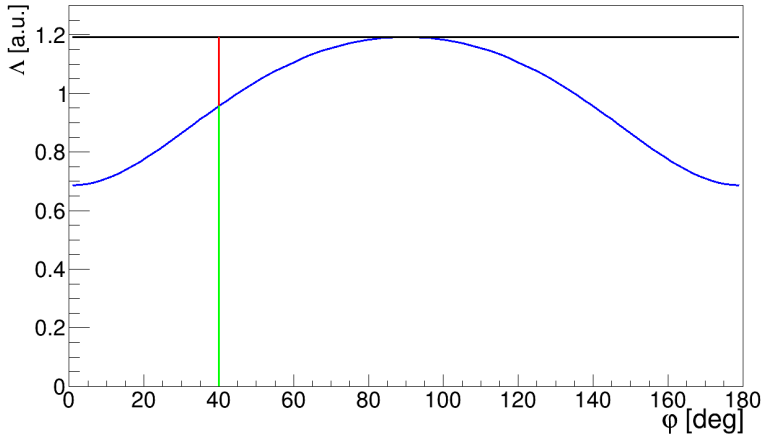

(a) Entanglement generation procedure for $\theta_1 = \theta_2 = 81.6°$.

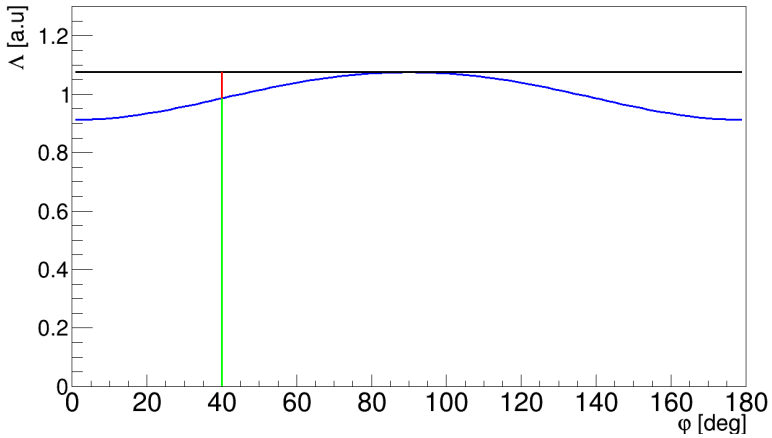

(b) Entanglement generation procedure for $\theta_1 = 40°$ and $\theta_2 = 70°$.

Figure 5.11: Entanglement generation procedure. For every event we calculate reconstructed Compton scattering angles θ_1, θ_2 and angle between scattering planes φ. Next we are calculating ratio function Λ (blue line) where we fix Compton scattering angles setting them to the values of reconstructed ones. Then we are generating random number $x \in U[0, \Lambda_{max}]$ (green and red lines) from a uniform distribution between 0 and maximum of the ratio function Λ_{max} (black line) and compare that value against value of the function Λ at reconstructed angle φ and if it's smaller (green line) we treat event as entangled.

Data analysis

6

6.1 Selections of events

Analysis chain of the measured data was the same as for the simulated one and goes as follows: first all the measured signals were grouped into events using J-PET Framework software and two selection criteria were introduced: first position of interaction along the scintillator strip should be in the active scintillating zone. As explained in chapter 5 length of the scintillator was 50cm. With coordinate system such that center of the scintillator was at $Z = 0$ and only those interaction for which $|Z| < 23cm$ were kept (Fig. 6.1).

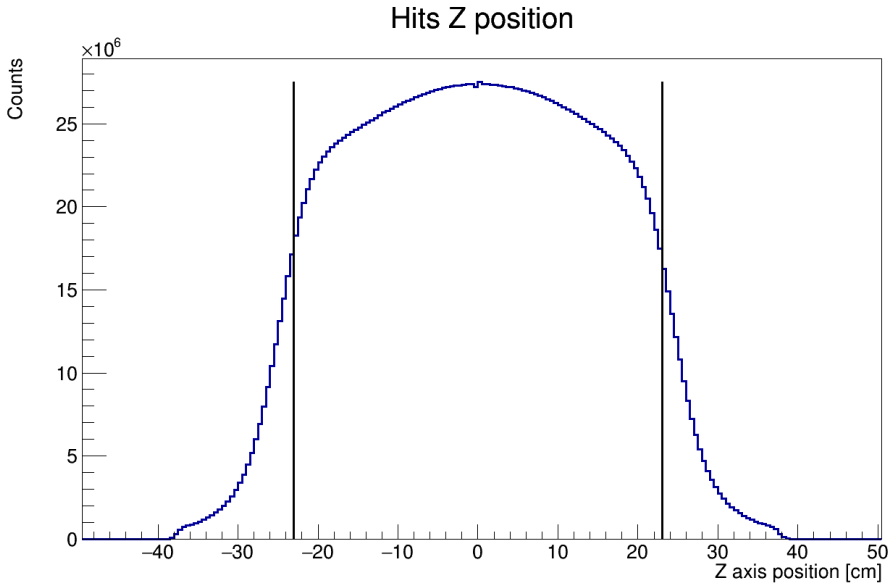

Figure 6.1: Z position of reconstructed interaction point. We are keeping for further analysis only those hits that were reconstructed in the active scintillator length, $|Z| <$ 23cm. Length of the scintillating strip was 50cm and ends of it were placed in metal frame to hold them in place. We are discarding events at the very ends of scintillating strip to remove any effects that could come from accidental scatterings in the frame.

Second selection criterium was based on energy deposition. J-PET detector does not measure energy deposition directly, however, as explained in chapter 4.2.1 time-over-threshold technique can be used to estimate energy deposition. Hits for which energy deposition was in range $E_{dep} \in (0.5ns, 19ns)$ were tagged as coming from positronium annihilaton and kept for further analysis (Fig. 6.2). After those two cuts events which contained exactly four hits were subjected to further analysis.

Next step was to find photons originating from para-positronium annihilation. We will once again use two times introduced in chapter 5 that is: t which is time of interaction and $\tau = t - \frac{d}{c}$ which is time of emission defined as time of interaction

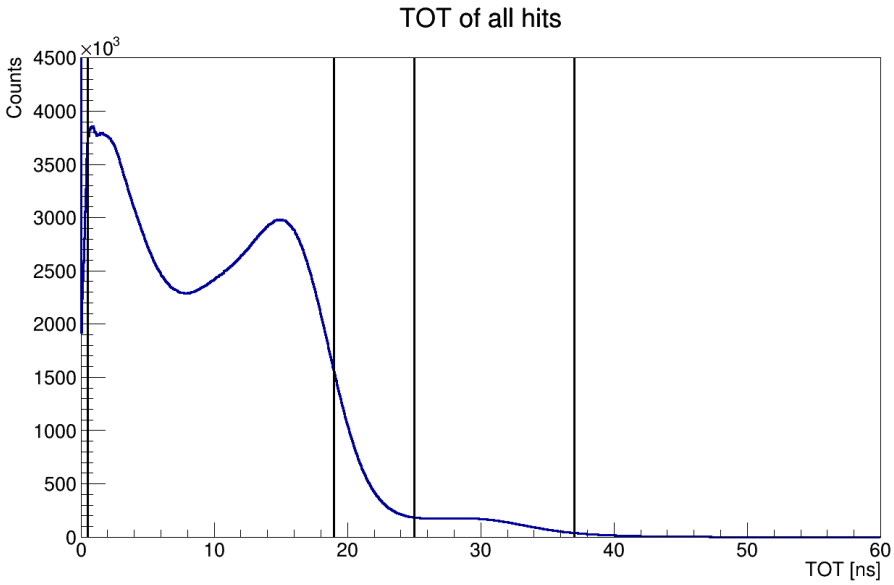

Figure 6.2: TOT of signal. J-PET detector does not measure energy deposited during a scattering directly, therefore different method had to be used to distinguish photons from positronia annihilations. As explained in chapter 4.2.1 time-over-threshold technique can be used to estimate energy deposition. Hits for which energy deposition was in range $E_{dep} \in (0.5ns, 19ns)$ were tagged as coming from positronium annihilaton and kept for further analysis

reduced by the time of flight (d is the distance between points of annihilation and interaction). For every pair of hits we are checking difference between those two times (Fig. 6.3) and assuming it could have been back-to-back hits if $|\tau_i - \tau_j| < 500ps$. For every pair of hits that passed this condition the position of annihilation point on the XY plane was calculated (Fig. 6.4) and if the position was within 1cm from the center of the detector also Z position of the annihilation point was calculated (Fig. 6.6). If that position is within $-4cm < Z < 4cm$, and only one pair of hits fulfilled all those conditions it's assumed to be a back-to-back pair.

After identifying back-to-back pair we are assigning scattered hits to the primary hits. We are again using parameter Δ_i defined in equation 5.2. Selection of correct scatterings once again made by creating plot of Δ_1 vs Δ_2 and elliptical cuts (parameters of which can be found in table 5.1) and assigning scattering to first or second primary interaction based on the position of the point: if it's in the lower-right ellipse scattering is assumed to come from first primary photon; if it's in upper-left ellipse it's assumed to come from second photon. After this selection procedure if exactly one photon was labeled as scattered from first primary and exactly one photon as scattered from second primary then all four interactions were found and distribution of Compton scattering angles as well as angle between scattering planes can be created (Fig. 6.8).

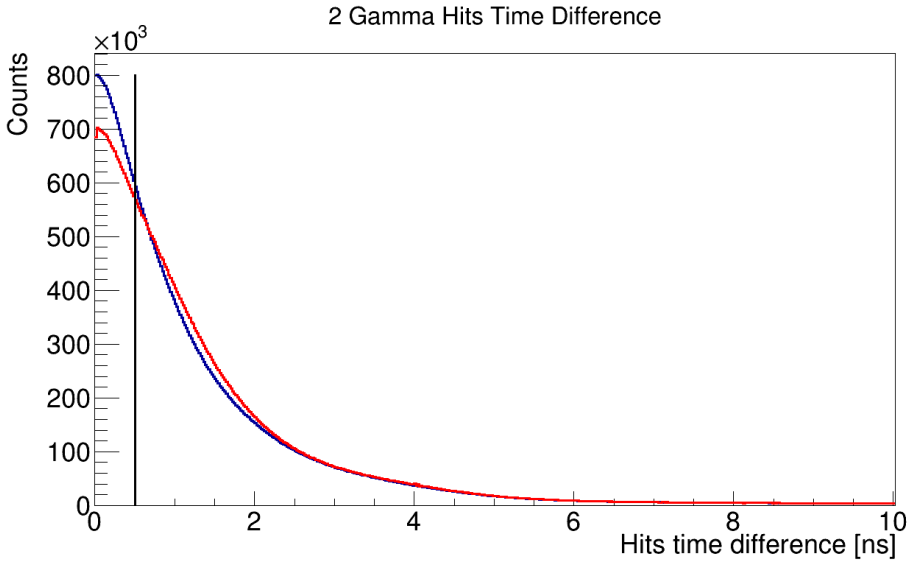

(a) Full spectrum of time difference between two hits.

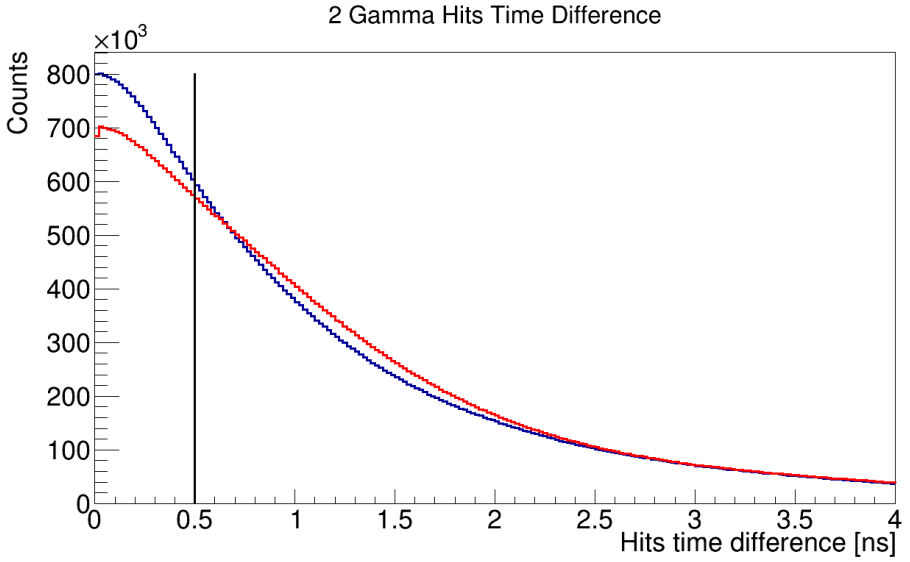

(b) Spectrum of time difference between two hits zoomed into an area of interest.

Figure 6.3: Time difference between every pair of hits. We are checking both time of interaction (blue line) and time of emission (red line) for each pair of hits within an event. If the time difference of interaction is lower than $500ps$ we are assuming that such pair can come from back-to-back decay therefore analyzing it further.

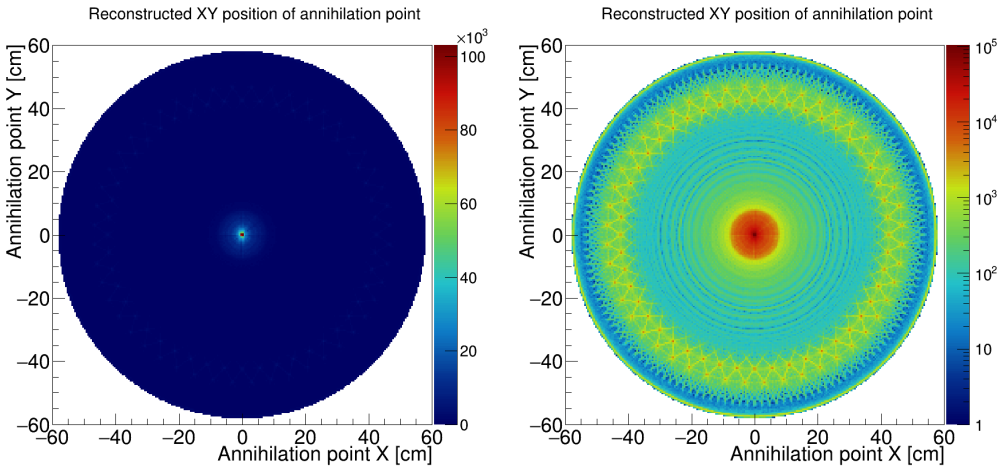

(a) Linear scale. **(b)** Logarithmic scale.

Figure 6.4: Reconstructed XY position of annihilation point. For every pair of hits that fulfilled previous conditions (that is position of interaction and time difference between interactions) position of annihilation point on the XY plane was calculated.

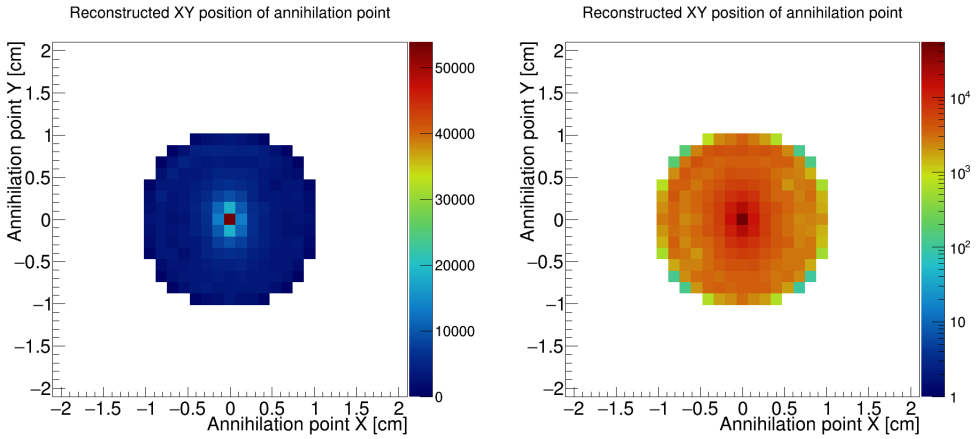

(a) Linear scale. **(b)** Logarithmic scale.

Figure 6.5: Selected annihilation points. If reconstructed XY position of annihilation point was closer than $1cm$ from the center of the detector we are assuming it came from back-to-back decay and analyze such pair further.

6.2 Efficiency corrections

Due to a geometry of the detector not all possible event configurations can be measured with the same efficiency. Therefore in order to compare measured data with theoretical distributions it is needed to implement correction on the detection efficiency. Those corrections were based on the same Monte Carlo simulations as described in chapter 5 using software developed by J-PET group based on Geant4 (described in chapter 4.3.2). It's design allows to track true information of the particles such as whether it's primary or scattered photon, first or second photon (described by internal numbers), photons momenta, interactions point and energy

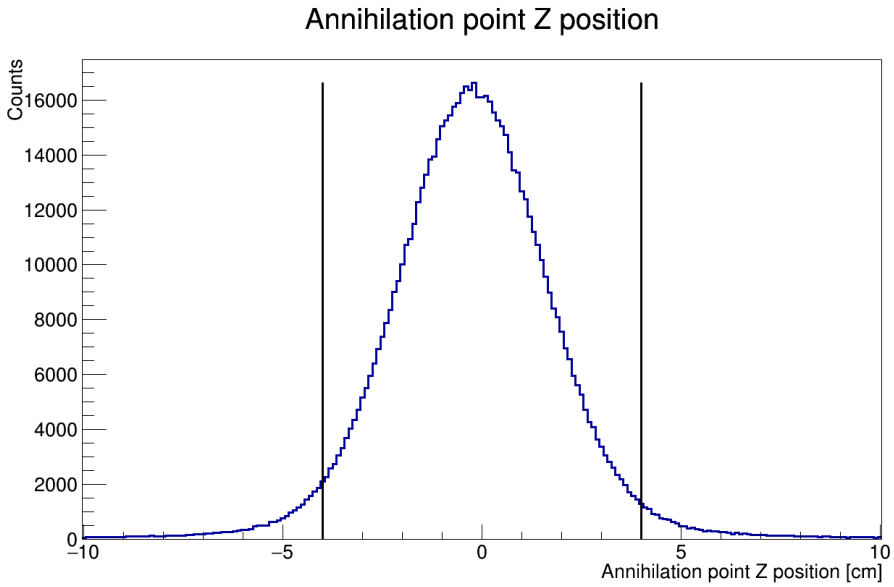

Figure 6.6: Reconstructed Z position of annihilation point. We are assuming that pair of hits came from back-to-back decay if $|Z| < 4cm$

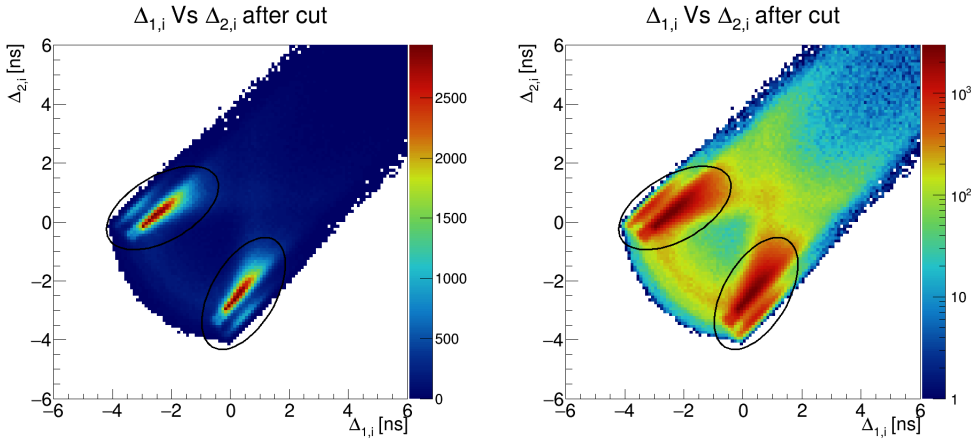

(a) Linear scale. **(b)** Logarithmic scale.

Figure 6.7: Scatter test. After identifying both primary photons we need to assign scattered photons to primary ones. It was done by calculating parameter Δ (see eq. 5.2). This parameters compares time it would took to photon to travel from point of primary interaction with time difference between two interactions. In the case of perfect measurement this parameter should be equal to zero if scattering comes from the primary interaction and different than zero when it did not (however wee need to account for experimental precision). To select correct scattering we are creating plot of Δ_1 vs Δ_2 and introduce elliptical cuts to assign scattering to first or second primary interaction (parameters of the ellipses can be found in table 5.18

deposition. Spectra for efficiency corrections were prepared in the following way: first, after both primary photons were detected the momenta of both scattered photons were registered and used to calculate the distribution of the angle between scattering planes regardless of whether scattered photons interacted in the detector. If both scattered photons interacted such event was labeled as "detected" and another

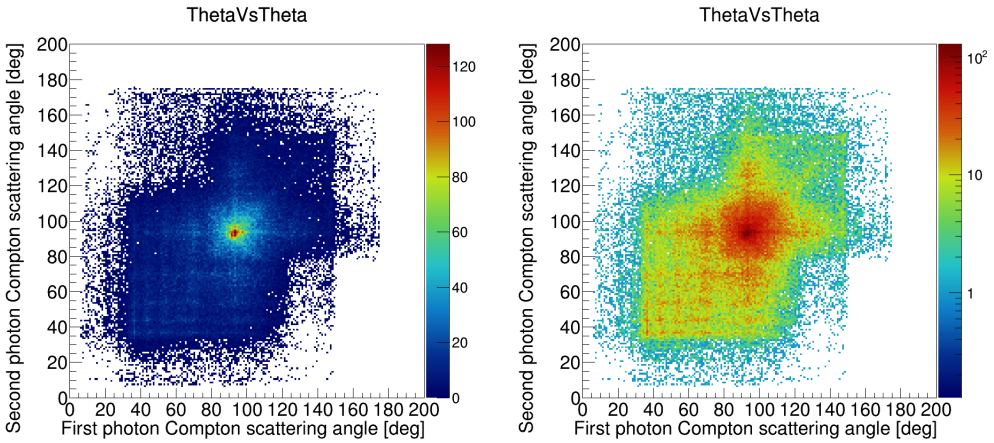

(a) Linear scale. **(b)** Logarithmic scale.

Figure 6.8: Distribution of reconstructed Compton scattering angles. After positively identifying both primary photons and assigning both scattered photons to their corresponding primary ones we are able to calculate Compton scattering angles.

distribution of an angle between scattering planes was created. Next step was to divide distribution labeled as "detected" by the distribution for all possible scatterings in order to get the distribution for the detection efficiency. Last step of applying efficiency corrections was to divide measured distribution of the angle between scattering planes by the efficiency function obtained in the previous step to obtain final distribution which can be compared with theoretical distribution for the angle between scattering planes. Efficiency distributions are plotted in Fig. 7.1.

6.3 Selection of scattered angle range

We are interested in the distribution of the angle between scattering planes in few different areas:

$$\begin{aligned} &\forall\theta_1,\theta_2 : \theta_1,\theta_2 \in [0,180]^\circ \\ &\forall\theta_1,\theta_2 : (\theta_1 - 82^\circ)^2 + (\theta_2 - 82^\circ)^2 < (30^\circ)^2 \\ &\forall\theta_1,\theta_2 : (\theta_1 - 100^\circ)^2 + (\theta_2 - 100^\circ)^2 < (30^\circ)^2 \\ &\forall\theta_1,\theta_2 : (\theta_1 - 92^\circ)^2 + (\theta_2 - 92^\circ)^2 < (10^\circ)^2 \end{aligned} \tag{6.1}$$

We are interested in all measured events as well as those that were inside three circles on θ_1 vs θ_2 plot - one around point $(82^\circ, 82^\circ)$ with radius of 30° which is centered around the point of maximum visibility in order to maximize interference contrast, one around $(92^\circ, 92^\circ)$ with radius of 10° and one around point $(100^\circ, 100^\circ)$ with radius of 30° - last two circles were chosen to maximize the number of measured events.

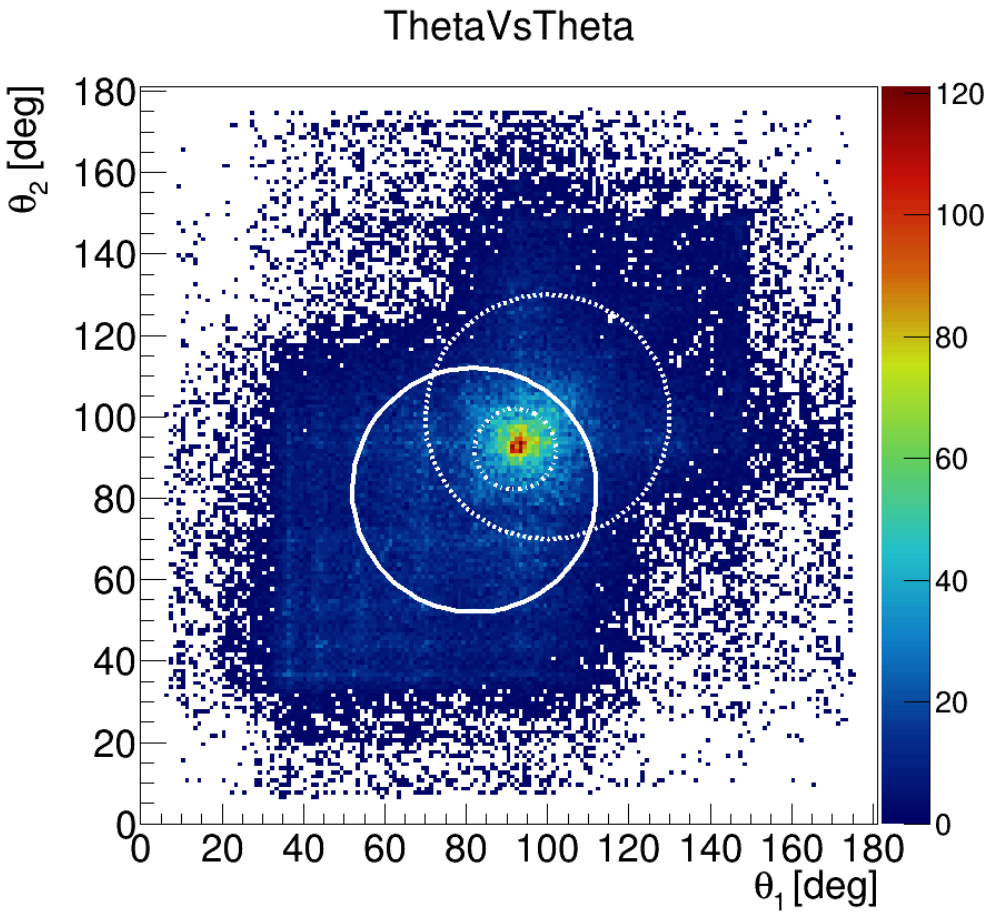

Figure 6.9: Areas of interest and distribution of measured Compton scattering angles. We have chosen four different areas in which we will determine the distribution of the angle between scattering planes - one for all measured events and those within three circle - one around point of highest visibility (white solid circle) and two to maximise number of measured events (white dotted lines).

Results

7

Efficiency corrections were applied to the measured data (efficiency distributions are presented in Fig. 7.1). Due to the design of the detector (as described in section 4.2) which is made of 192 single scintillating strips (see Fig. 4.2). Design like that offers limited angular coverage which results in lower efficiency detection for some configurations of angles between scattering planes therefore showing irregularities in the efficiency detection functions.

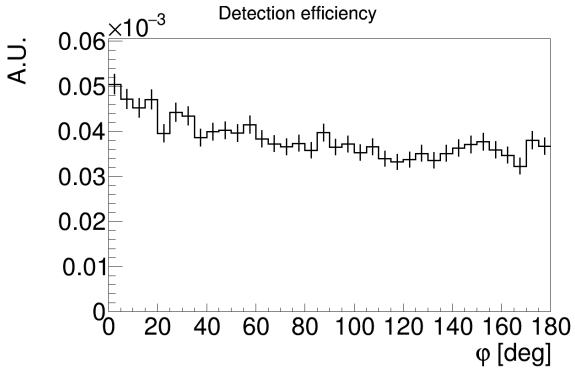

(a) Detection efficiency as a function of angle between scattering planes for all measured events.

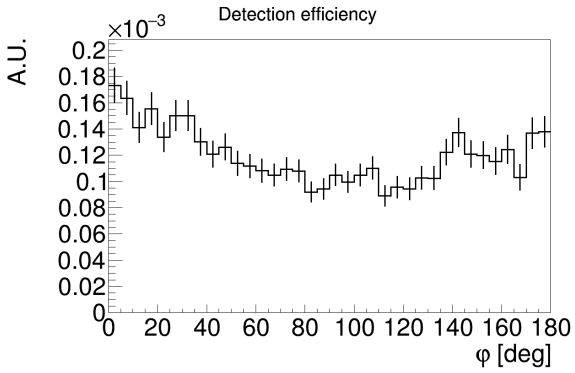

(b) Detection efficiency as a function of angle between scattering planes for events in circle around $(82°, 82°)$ with radius of $30°$.

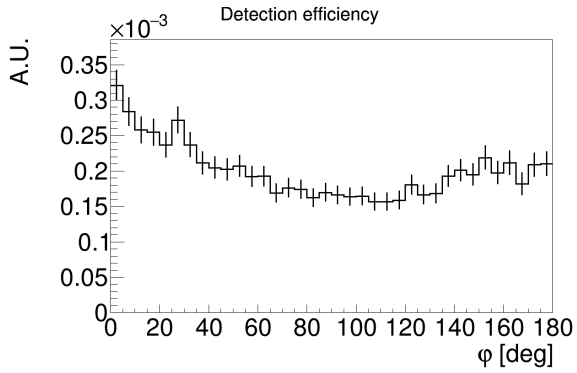

(c) Detection efficiency as a function of angle between scattering planes for events in circle around $(100°, 100°)$ with radius of $30°$

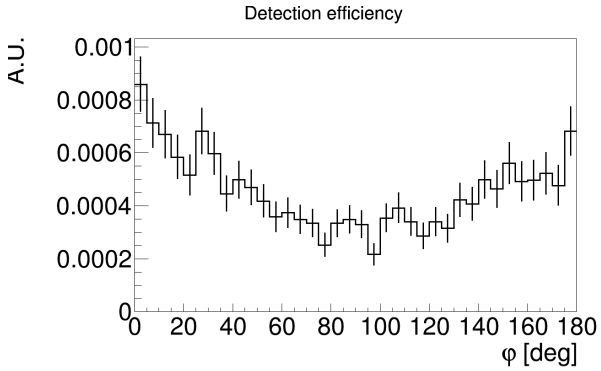

(d) Detection efficiency as a function of angle between scattering planes for events in circle around $(92°, 92°)$ with radius of. $10°$

Figure 7.1: Detection efficiency as a function of angle between scattering planes for events in four different area of interest.

After applying efficiency corrections distributions of the angle between scattering planes were created and plotted against two hypotheses - that photons from para-positronium decay are entangled (as described by equation 3.20) and that they are separable (described by equation 3.21). Those plots are presented in Fig. 7.2 where reconstructed results are marked by the black line, hypothesis that photons are entangled is marked by the green line and hypothesis that they are separable by the blue line.

In order to quantify the similarity between reconstructed distribution and distributions for both of the hypotheses χ^2 test was performed and results of this test can be found in table 7.1 where the numbers are χ^2 per numbers of degrees of freedom.

As can be seen from table 7.1 results of the measurement are more consistent with the assumption that photons from para-positronium decays are entangled and differ significantly with the assumption that they are separable.

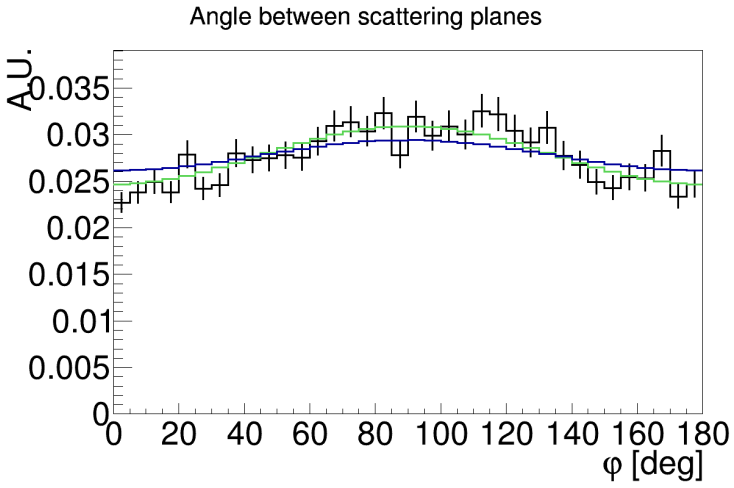

(a) Distribution of the angle between scattering planes for all measured events.

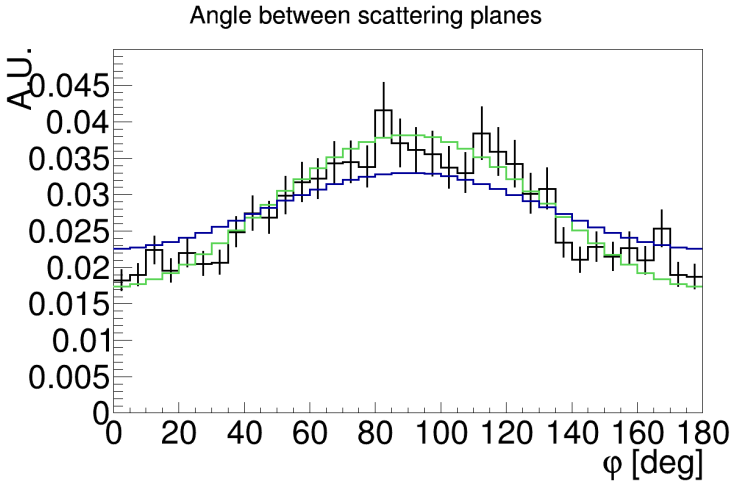

(b) Distribution of the angle between scattering planes for events in circle around $(82°, 82°)$ with radius of $30°$.

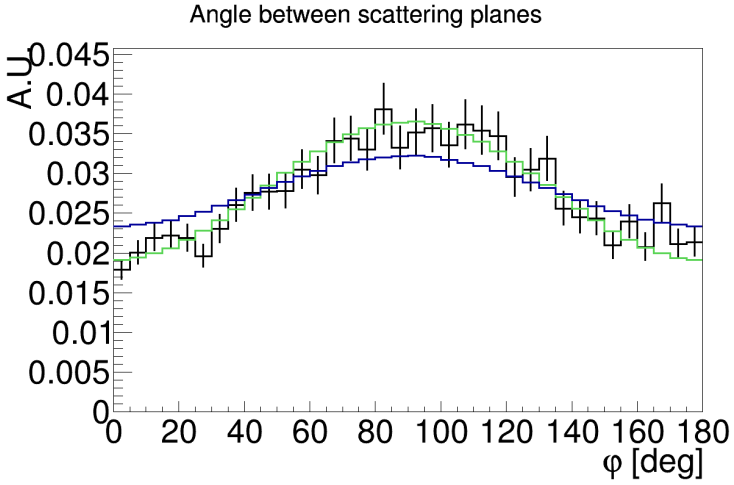

(c) Distribution of the angle between scattering planes for events in circle around $(100°, 100°)$ with radius of $30°$

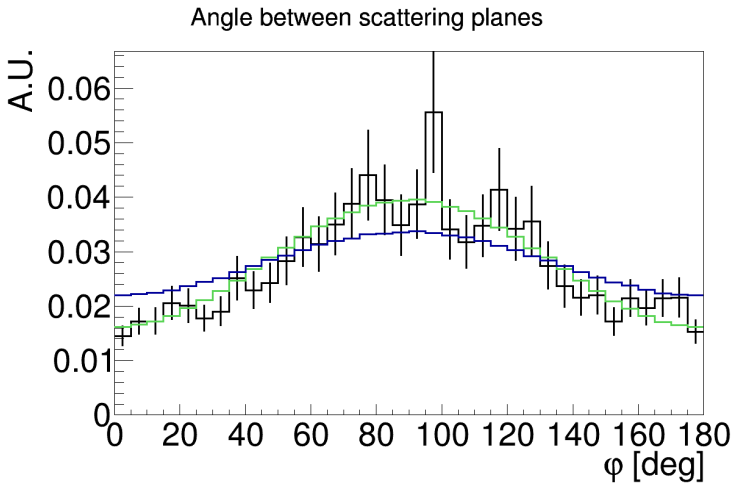

(d) Distribution of the angle between scattering planes for events in circle around $(92°, 92°)$ with radius of. $10°$

Figure 7.2: Distribution of the angle between scattering planes for events in four different area of interest. Black line represents reconstructed angles between scattering planes and is compared against two hypotheses - that the photons from para-positronium annihilation are entangled (green line) and that they are separable (blue line).

	Hypothesis of entangled states	Hypothesis of separable states
All Compton scattering angles	1.025	1.937
Circle around $(82°, 82°)$ and $R < 30°$	1.048	2.442
Circle around $(100°, 100°)$ and $R < 30°$	0.829	2.246
Circle around $(92°, 92°)$ and $R < 10°$	0.667	2.161

Table 7.1: Results of the χ^2 test comparing reconstructed data against two hypotheses - that the state is entangled and that it is separable. Values in the table are χ^2 per number of degrees of freedom.

Discussion and perspectives

8

Studies presented in this thesis concern the measurement of the distribution of the angle between scattering planes of two photons originating from para-positronim decays using J-PET detector. We have performed extensive studies of the distribution of the angle between scattering planes in a broad spectrum of possible Compton scattering angles. We have performed Monte Carlo simulations of the para-positronium decays and propagation of photons in the J-PET detector with two different assumptions - that photons from the dacays are in the entangled state and that they are in a separable one. We have used those results to obtain detector response function for the detection of double Compton scatterings and to establish selection criteria for the measured data. We have then performed an experiment in which source of sodium sandwiched between porous material was placed in the center of J-PET detector producing e^+e^- decays of which were measured. Measured data were then corrected by simulated detection efficiency and compared against theoretical distributions for the angle between scattering planes obtained under two assumptions - that the decaying state was entangled and that it was separable. We have shown that measured results are with a better agreement with theoretically predicted ones under assumption that decaying state was entangled but differ significantly with the assumptions that they were separable. We have shown that the J-PET detector is capable of a measurement of relative polarisations of photons which can be used in various future investigations such as discreete symmetries breaking or background suppression in positron emission tomography.

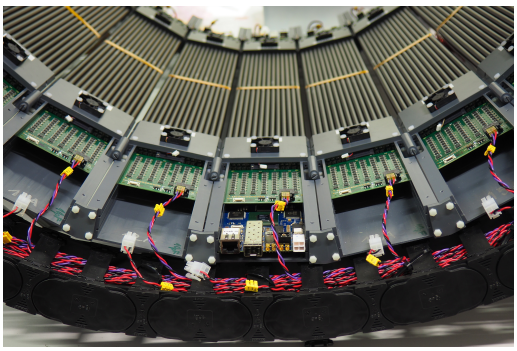

(a) Close-up view of the scintillating modules. Each module consists of 13 scintillators of size $500 \times 24 \times 6$ mm^3 and is read out by silicon photomultipliers connected to a rad out board on each side.

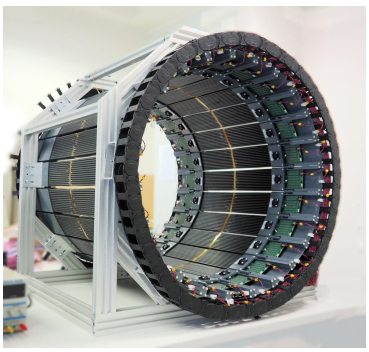

(b) View of assembled detector. It is build with 24 scintillating modules arranged concentrically.

Figure 8.1: Next generation of J-PET detector, made of 24 scintillating modules.

Results obtained in this thesis can be further improved by performing a measurement on newest iteration of the J-PET detector, called Modular J-PET, which instead of 192 single scintillating strips, is build out of 24 independent scintillating

modules, each module consisting of 13 scintillators of size $500 \times 24 \times 6mm^3$ [71]. Design like that offers few advantages over a previous one such as much bigger angular coverage improving detection efficiency therefore improving the analysis of the measurement of the angle between scattering planes. In addition modular design allows to freely add or remove modules, therefore changing the radius of the detector.

Bibliography

[1] Moskal, P., Alfs, D., Bednarski, T., [...], **Krawczyk, N.**, et al., Potential of the J-PET Detector for Studies of Discrete Symmetries in Decays of Positronium Atom — A Purely Leptonic System. *Acta Physica Polonica B* **47**, 509 (2016).

[2] Acín, A., Latorre, J. I., Pascual, P., Three-party entanglement from positronium. *Physical Review A* **63**, 042107 (2001).

[3] Hiesmayr, B. C., Moskal, P., Genuine Multipartite Entanglement in the 3-Photon Decay of Positronium. *Scientific Reports* **7**, 15349 (2017).

[4] Hiesmayr, B. C., Moskal, P., Witnessing Entanglement In Compton Scattering Processes Via Mutually Unbiased Bases. *Scientific Reports* **9**, 8166 (2019).

[5] Nowakowski, M., Fierro, D. B., Three-photon Entanglement from Ortho-Positronium Revisited. *Acta Physica Polonica B* **48**, 1955 (2017).

[6] Spengler, C., Huber, M., Brierley, S., et al., Entanglement detection via mutually unbiased bases. *Physical Review A* **86**, 022311 (2012).

[7] Sharma, S., Kumar, D., and, P. M., Decoherence Puzzle in Measurements of Photons Originating from Electron-Positron Annihilation. *Acta Physica Polonica A* **142**, 428–435 (2022).

[8] Watts, D. P., Bordes, J., Brown, J. R., et al., Photon quantum entanglement in the MeV regime and its application in PET imaging. *Nature Communications* **12**, 2646 (2021).

[9] Abdurashitov, D., Baranov, A., Borisenko, D., et al., Setup of Compton polarimeters for measuring entangled annihilation photons. *Journal of Instrumentation* **17**, P03010 (2022).

[10] Makek, M., Bosnar, D., Pavelić, L., et al., Single-layer Compton detectors for measurement of polarization correlations of annihilation quanta. *Nuclear Instruments and Methods in Physics Research Section A: Accelerators, Spectrometers, Detectors and Associated Equipment* **958**, 162835 (2020).

[11] Parashari, S., Bosnar, D., Friščić, I., et al., *Closing the Door on the "Puzzle of Decoherence" of Annihilation Quanta*, 2023, arXiv: `2304.11362 [quant-ph]`.

[12] Moskal, P., Niedźwiecki, S., Bednarski, T., et al., Test of a single module of the J-PET scanner based on plastic scintillators. *Nuclear Instruments and Methods in Physics Research Section A: Accelerators, Spectrometers, Detectors and Associated Equipment* **764**, 317–321 (2014).

[13] Moskal, P., Zoń, N., Bednarski, T., et al., A novel method for the line-of-response and time-of-flight reconstruction in TOF-PET detectors based on a library of synchronized model signals. *Nuclear Instruments and Methods in Physics Research Section A: Accelerators, Spectrometers, Detectors and Associated Equipment* **775**, 54–62 (2015).

[14] Moskal, P., Rundel, O., Alfs, D., et al., Time resolution of the plastic scintillator strips with matrix photomultiplier readout for J-PET tomograph. *Physics in Medicine and Biology* **61**, 2025–2047 (2016).

[15] Raczyński, L., Wiślicki, W., Krzemień, W., [. . .], **Krawczyk, N.**, et al., Calculation of the time resolution of the J-PET tomograph using kernel density estimation. *Physics in Medicine and Biology* **62**, 5076–5097 (2017).

[16] Moskal, P., Kisielewska, D., Curceanu, C., et al., Feasibility study of the positronium imaging with the J-PET tomograph. *Physics in Medicine and Biology* **64**, 055017 (2019).

[17] Moskal, P., Dulski, K., Chug, N., [. . .], **Krawczyk, N.**, et al., Positronium imaging with the novel multiphoton PET scanner. *Science Advances* **7**, eabh4394 (2021).

[18] Moskal, P., Gajos, A., Mohammed, M., [. . .], **Krawczyk, N.**, et al., Testing CPT symmetry in ortho-positronium decays with positronium annihilation tomography. *Nature Communications* **12**, 5658 (2021).

[19] Niedźwiecki, S., Białas, P., Curceanu, C., [. . .], **Krawczyk, N.**, et al., J-PET: A New Technology for the Whole-body PET Imaging. *Acta Physica Polonica B* **48**, 1567 (2017).

[20] Pałka, M., Strzempek, P., Korcyl, G., et al., Multichannel FPGA based MVT system for high precision time (20 ps RMS) and charge measurement. *Journal of Instrumentation* **12**, P08001–P08001 (2017).

[21] Korcyl, G., Hiesmayr, B. C., Jasinska, B., [. . .], **Krawczyk, N.**, et al., Evaluation of Single-Chip, Real-Time Tomographic Data Processing on FPGA SoC Devices. *IEEE Transactions on Medical Imaging* **37**, 2526–2535 (2018).

[22] Krzemień, W., Alfs, D., Białas, P., et al., Overview of the Software Architecture and Data Flow for the J-PET Tomography Device. *Acta Physica Polonica B* **47**, 561 (2016).

[23] Krzemien, W., Gajos, A., Kacprzak, K., et al., J-PET Framework: Software platform for PET tomography data reconstruction and analysis. *SoftwareX* **11**, 100487 (2020).

[24] Moskal, P., **Krawczyk, N.**, Hiesmayr, B. C., et al., Feasibility studies of the polarization of photons beyond the optical wavelength regime with the J-PET detector. *The European Physical Journal C* **78**, 970 (2018).

[25] Wheeler, J. A., Polyelectrons. *Annals of the New York Academy of Sciences* **48**, 219–238 (1946).

[26] Klein, O., Nishina, Y., Über die Streuung von Strahlung durch freie Elektronen nach der neuen relativistischen Quantendynamik von Dirac. *Zeitschrift für Physik* **52**, 853–868 (1929).

[27] Pryce, M. H. L., Ward, J. C., Angular Correlation Effects with Annihilation Radiation. *Nature* **160**, 435–435 (1947).

[28] Snyder, H. S., Pasternack, S., Hornbostel, J., Angular Correlation of Scattered Annihilation Radiation. *Physical Review* **73**, 440–448 (1948).

[29] Bleuler, E., Bradt, H. L., Correlation between the States of Polarization of the Two Quanta of Annihilation Radiation. *Physical Review* **73**, 1398–1398 (1948).

[30] Hanna, R. C., Polarization of Annihilation Radiation. *Nature* **162**, 332–332 (1948).

[31] Wu, C. S., Shaknov, I., The Angular Correlation of Scattered Annihilation Radiation. *Physical Review* **77**, 136–136 (1950).

[32] Langhoff, H., Die Linearpolarisation der Vernichtungsstrahlung von Positronen. *Zeitschrift für Physik* **160**, 186–193 (1960).

[33] Kasday, L. R., Ullman, J., Wu, C. S., Angular correlation of compton-scattered annihilation photons and hidden variables. *Il Nuovo Cimento B Series 11* **25**, 633–661 (1975).

[34] Bohm, D., Aharonov, Y., Discussion of Experimental Proof for the Paradox of Einstein, Rosen, and Podolsky. *Physical Review* **108**, 1070–1076 (1957).

[35] Einstein, A., Podolsky, B., Rosen, N., Can Quantum-Mechanical Description of Physical Reality Be Considered Complete? *Physical Review* **47**, 777–780 (1935).

[36] Wilson, A. R., Lowe, J., Butt, D. K., Measurement of the relative planes of polarization of annihilation quanta as a function of separation distance. *Journal of Physics G: Nuclear Physics* **2**, 613–624 (1976).

[37] McNamara, A. L., Toghyani, M., Gillam, J. E., et al., Towards optimal imaging with PET: aniin silico/ifeasibility study. *Physics in Medicine and Biology* **59**, 7587–7600 (2014).

[38] Toghyani, M., Gillam, J. E., McNamara, A. L., et al., Polarisation-based coincidence event discrimination: aniin silico/istudy towards a feasible scheme for Compton-PET. *Physics in Medicine and Biology* **61**, 5803–5817 (2016).

[39] Knights, P., Ryburn, F., Tungate, G., et al., Studying the effect of polarisation in Compton scattering in the undergraduate laboratory. *European Journal of Physics* **39**, 025203 (2018).

[40] Caradonna, P., Reutens, D., Takahashi, T., et al., Probing entanglement in Compton interactions. *Journal of Physics Communications* **3**, 105005 (2019).

[41] Parashari, S., Bokulić, T., Bosnar, D., et al., Optimization of detector modules for measuring gamma-ray polarization in Positron Emission Tomography. *Nuclear Instruments and Methods in Physics Research Section A: Accelerators, Spectrometers, Detectors and Associated Equipment* **1040**, 167186 (2022).

[42] Deutsch, M., Evidence for the Formation of Positronium in Gases. *Physical Review* **82**, 455–456 (1951).

[43] Karshenboim, S. G., Precision study of positronium: testing bound state QED theory. *International Journal of Modern Physics A* **19**, 3879–3896 (2004).

[44] Al-Ramadhan, A. H., Gidley, D. W., New precision measurement of the decay rate of singlet positronium. *Physical Review Letters* **72**, 1632–1635 (1994).

[45] Bass, S., QED and Fundamental Symmetries in Positronium Decays. *Acta Physica Polonica B* **50**, 1319 (2019).

[46] Vetter, P. A., Freedman, S. J., Branching-ratio measurements of multiphoton decays of positronium. *Physical Review A* **66**, 052505 (2002).

[47] Vallery, R. S., Zitzewitz, P. W., Gidley, D. W., Resolution of the Orthopositronium-Lifetime Puzzle. *Physical Review Letters* **90**, 203402 (2003).

[48] Greenberger, D. M., Horne, M. A., Shimony, A., et al., Bell's theorem without inequalities. *American Journal of Physics* **58**, 1131–1143 (1990).

[49] Bell, J. S., On the Einstein Podolsky Rosen paradox. *Physics Physique* **1**, 195–200 (1964).

[50] Clauser, J. F., Shimony, A., Bell's theorem. Experimental tests and implications. *Reports on Progress in Physics* **41**, 1881–1927 (1978).

[51] Aspect, A., Dalibard, J., Roger, G., Experimental Test of Bell's Inequalities Using Time- Varying Analyzers. *Physical Review Letters* **49**, 1804–1807 (1982).

[52] Tittel, W., Brendel, J., Zbinden, H., et al., Violation of Bell Inequalities by Photons More Than 10 km Apart. *Physical Review Letters* **81**, 3563–3566 (1998).

[53] Zuber, J.-B., Itzykson, C., *Quantum Field Theory*, English (Dover Publications, Paperback, 2006), p. 752, ISBN: 978-0486445687.

[54] Clauser, J. F., Horne, M. A., Shimony, A., et al., Proposed Experiment to Test Local Hidden-Variable Theories. *Physical Review Letters* **23**, 880–884 (1969).

[55] Kamińska, D., Gajos, A., Czerwiński, E., [...], **Krawczyk, N.**, et al., A feasibility study of ortho-positronium decays measurement with the J-PET scanner based on plastic scintillators. *The European Physical Journal C* **76**, 445 (2016).

[56] Thirolf, P., Lang, C., Parodi, K., Perspectives for Highly-Sensitive PET-Based Medical Imaging Using sup/sup Coincidences. *Acta Physica Polonica A* **127**, 1441–1444 (2015).

[57] Schultz, P. J., Lynn, K. G., Interaction of positron beams with surfaces, thin films, and interfaces. *Reviews of Modern Physics* **60**, 701–779 (1988).

[58] Puska, M. J., Nieminen, R. M., Theory of positrons in solids and on solid surfaces. *Reviews of Modern Physics* **66**, 841–897 (1994).

[59] Gorgol, M., Jasińska, B., Kosior, M., et al., Construction of the Vacuum Chambers for J-PET Experiments with Positron Annihilation. *Acta Physica Polonica B* **51**, 293 (2020).

[60] Moskal, P., Stępień, E. Ł., Prospects and Clinical Perspectives of Total-Body PET Imaging Using Plastic Scintillators. *PET Clinics* **15**, 439–452 (2020).

[61] Moskal, P., Kowalski, P., Shopa, R. Y., [...], **Krawczyk, N.**, et al., Simulating NEMA characteristics of the modular total-body J-PET scanner—an economic total-body PET from plastic scintillators. *Physics in Medicine and Biology* **66**, 175015 (2021).

[62] Gajos, A., Curceanu, C., Czerwiński, E., et al., Feasibility Study of the Time Reversal Symmetry Tests in Decay of Metastable Positronium Atoms with the J-PET Detector. *Advances in High Energy Physics* **2018**, 1–10 (2018).

[63] Czerwiński, E., Dulski, K., Białas, P., [...], **Krawczyk, N.**, et al., Commissioning of the J-PET Detector for Studies of Decays of Positronium Atoms. *Acta Physica Polonica B* **48**, 1961 (2017).

[64] Moskal, P., Niedźwiecki, S., Bednarski, T., et al., Test of a single module of the J-PET scanner based on plastic scintillators. *Nuclear Instruments and Methods in Physics Research Section A: Accelerators, Spectrometers, Detectors and Associated Equipment* **764**, 317–321 (2014).

[65] Vandenberghe, S., Moskal, P., Karp, J. S., State of the art in total body PET. *EJNMMI Physics* **7**, 35 (2020).

[66] Sharma, N., Silarski, M., Chhokar, J., [...], **Krawczyk, N.**, et al., Hit-Time and Hit-Position Reconstruction in Strips of Plastic Scintillators Using Multithreshold Readouts. *IEEE Transactions on Radiation and Plasma Medical Sciences* **4**, 528–537 (2020).

[67] Sharma, S., TOT Method for the Disentanglement of Photons in Positron Annihilation Lifetime Spectroscopy. *Acta Physica Polonica A* **137**, 130–133 (2020).

[68] Moskal, P., Bednarski, T., Białas, P., et al., Strip- PET: a novel detector concept for the TOF-PET scanner. *Nuclear Medicine Review* **15**, 68–69 (2012).

[69] Agostinelli, S., Allison, J., Amako, K., et al., Geant4—a simulation toolkit. *Nuclear Instruments and Methods in Physics Research Section A: Accelerators, Spectrometers, Detectors and Associated Equipment* **506**, 250–303 (2003).

[70] Jan, S., Santin, G., Strul, D., et al., GATE: a simulation toolkit for PET and SPECT. *Physics in Medicine and Biology* **49**, 4543–4561 (2004).

[71] Sharma, S., Baran, J., Brusa, R., et al., J-PET detection modules based on plastic scintillators for performing studies with positron and positronium beams. *Journal of Instrumentation* **18**, C02027 (2023).